Design and characterisation of a bi-modal solar thermal propulsion and power system for small satellites

Leverone, Fiona; Cervone, Angelo; Pini, Matteo; Gill, Eberhard

DOI
10.1016/j.applthermaleng.2021.116609

Publication date
2021

Document Version
Final published version

Published in
Applied Thermal Engineering

Applied Thermal Engineering 189 (2021) 116609

Contents lists available at ScienceDirect

Applied Thermal Engineering

journal homepage: www.elsevier.com/locate/apthermeng

Design and characterisation of a bi-modal solar thermal propulsion and power system for small satellites

Fiona Leverone [a,b,*], Angelo Cervone [b], Matteo Pini [a], Eberhard Gill [b]

[a] Department of Propulsion and Power, Delft University of Technology, Kluyverweg 1, 2629 HS Delft, the Netherlands
[b] Department of Space Systems Engineering, Delft University of Technology, Kluyverweg 1, 2629 HS Delft, the Netherlands

ARTICLE INFO

Keywords:
Mini-satellites
Solar concentration
Ultra-high temperatures
Silicon phase change material

ABSTRACT

Small satellites with increased capabilities in terms of power and propulsion are being demanded for future missions. This paper addresses an alternative bi-modal solution which consists of a solar thermal propulsion system coupled with a micro-Organic Rankine Cycle system, to co-generate thrust and electrical power. Current literature on bi-modal systems is limited to static power conversion systems such as thermionic conversion processes. Therefore, this paper expands the research of bi-modal systems to dynamic power conversion systems and latent heat storage systems. The paper documents the design process, key design parameters, and feasibility of this system for a Geostationary Transfer Orbit to Lunar Orbit insertion mission. The results of a single-objective optimisation show the system is most suitable on-board small satellites with a gross mass above 300 kg. The propellant accounts for 50% of the total system mass. The final design uses Silicon as the latent heat energy storage system due to its high specific energy of more than 250 Wh/kg. Additionally, the enthalpy method is used to describe the dynamic behaviour of the phase change material and results show the insulation thermal conductivity has the largest effect, up to 17%, on the receiver's maximum achievable steady-state temperature.

1. Introduction

The increase of electrical power and shorter transfer time requirements of future interplanetary small spacecraft promotes the need for efficient, low mass, and high-performing propulsion and power systems. In terms of power generation, target power densities and specific energies are estimated to be between 150 and 250 W/kg [1] and more than 250 Wh/kg [2] respectively. Current state-of-the-art photovoltaic technologies for small satellites are around 20 to 100 W/kg [3,4] and Lithium-polymer and –ion batteries have specific energies between 150 and 250 Wh/kg. These systems are currently below the targeted values and call for alternative systems to be investigated.

Electric propulsion systems are commonly used for interplanetary missions due to their high specific impulse values. However, they may not be appropriate for missions that require short transfer times on-board small spacecraft that have limited electrical power budgets due to their low thrust and high-power consumption. Solar thermal propulsion (STP) has been identified as a promising candidate for these high-velocity increment missions [5–7]. STP is an advance propulsion system, that focuses solar radiation using mirrors or lenses to heat the propellant to very high temperatures, generally between 1000 and 2500 K, to achieve high specific impulse values of 790 s [8]. The vaporised propellant is expanded through a nozzle to generate thrust. These systems are capable of achieving high-energy conversion efficiencies of 50–80% [9].

Previous bi-modal studies have coupled STP or nuclear propulsion systems with static power generation systems such as thermionic [10–16] and thermophotovoltaic [17] power conversion systems in order to achieve efficient bi-modal systems. The thermionic conversion process operates by transferring electrons from a hot emitter through a vacuum to a cooler collector to generate electricity. However, [18,19] show that these systems are more suitable for larger power levels. Thermophotovoltaic conversion systems consist of photovoltaic cells that convert infrared radiation from a hot thermal emitter into electricity. Disadvantages of photovoltaic cells are that they are vulnerable to degradation in the space environment [20,21] and have low power to mass ratios [18,19]. Although, it is expected that substantial improvement in the power density ratio from the current 15 W/kg is possible, as was the case with conventional photovoltaic systems [18,22].

An alternative to theses static systems is the use of dynamic power conversion systems that have the potential to offer improved solar-to-electric efficiency, potential cost-saving and longer life expectancy in

* Corresponding author at: Department of Propulsion and Power, Delft University of Technology, Kluyverweg 1, 2629 HS Delft, the Netherlands.
E-mail addresses: F.K.Leverone@tudelft.nl (F. Leverone), A.Cervone@tudelft.nl (A. Cervone), M.Pini@tudelft.nl (M. Pini), E.K.A.Gill@tudelft.nl (E. Gill).

https://doi.org/10.1016/j.applthermaleng.2021.116609
Received 21 July 2020; Received in revised form 7 October 2020; Accepted 17 January 2021
Available online 8 February 2021

harsh radiation environments [23,18]. The dynamic power conversion system under investigation in this study is the micro-organic Rankine Cycle (ORC) system. Here micro refers to power levels on the order of 100 W to 500 W. ORC turbogenerators are thermal engines capable of converting thermal energy into electrical power by means of an organic fluid evolving in a closed-loop based on the classical Rankine thermodynamic cycle. The organic working fluid undergoes a phase change to drive a turbine and generate electricity [24–26].

The concept of using ORC systems for power generation in space dates back to the 1960s, where ORC systems were proposed to power the International Space Station with power capacities ranging from 1 to 50 kW [23,27,28]. In general, Rankine cycles can have higher thermal efficiencies compared to Brayton and Stirling cycles in the space environment at the expense of larger radiators [29].

At micro-scales, Rankine cycles can also have better thermal efficiency [18] and higher power density compared to micro-Brayton cycles [30]. The lower performance of micro-Brayton cycles is due to the poor cycle efficiency as a result of miniaturising the system which allows high heat conduction from the turbine to the compressor. Therefore, micro-ORC systems could result in designs that are smaller in volume and mass, which are critical design criteria for small satellites.

ORC systems provide lower turbine rotational speeds, larger turbine designs, and lower freezing temperatures compared to conventional Rankine cycles, and the organic fluid can also act as lubricant [31,23,32]. These advantages decrease the system maintenance of ORC systems to once per year for terrestrial applications [33]. It could be plausible to extend the operational time to a few years to meet the operational life-span of a small spacecraft. Another benefit of a micro-ORC system is its higher resistance to degradation compared to photovoltaic systems [23,27,34]. In terrestrial applications, the minimum ORC pressure has to be greater than atmospheric pressure to avoid air leakage into the system. This is not a concern in this design due to vacuum ambient conditions.

Micro-ORCs also have numerous drawbacks such as a lack of space heritage, which increases the risk of the system, and they have lower reliability due to moving parts compared to static power systems. Additional disadvantages are the fast rotational speeds of the turbine (up to 1000000 rpm), potential transient inertial effects during start-up and shut-down, leakages, cooling of components, micro-gravity operation of two-phase flow, and large radiator surface areas [31,35,36]. The ultra-fast rotational speed is arguably a source of failure of the bi-modal system and future work on micro-turbine design is required, especially pertaining to the thermal management due to the high surface to volume ratio of the turbine and the speed of the bearings. Though, current experimental work on high-speed radial compressor designs, with rotational speeds greater than 200000 rpm, [37,38], could benefit small radial turbine designs due to shared technical solutions that can be adopted by both these turbomachines. In terms of torque, the small size and low mass of the turbine combined with the ultra-fast rotational speed results in low torque values of approximately 2 mNm. These values are below values of typical small satellite reaction wheels (10–210 mNm) [39].

Improving system efficiency and reducing the mass of the proposed novel bi-modal system is necessary to ensure the system is feasible and cost-competitive.The design of the bi-modal solar thermal propulsion system is, therefore, challenging and requires an integrated design approach already at the conceptual and preliminary design phase. However, there is currently no literature available on the design process of the proposed bi-modal system. Additionally, the influence of design parameters on the proposed integrated solar thermal system is unknown. Therefore this paper extends the research of bi-modal STP systems to dynamic power conversion systems and focuses on the design overview of the integrated system as well as provides guidelines for future evaluations to address the gap in literature. The design approach is combined to a genetic algorithm for the optimal exploration of the design space to minimise the wet system mass of the bi-modal system while meeting the thermal energy storage requirement. The optimisation is conducted for various mini-spacecraft, which are classified as having a gross mass between 100 and 500 kg, to identify the feasibility and optimal spacecraft mass for this system. A Geostationary Transfer Orbit (GTO) to Lunar orbit mission has been selected based on [40,41]. A summary of the essential system requirements for the selected mission along with their corresponding rationale is provided in Table 1 [41].

Moreover, most bi-modal STP systems incorporate sensible energy storage systems [13–15,6] except for that proposed by [17], which uses latent energy storage. Therefore, this work contributes to expanding the limited knowledge on the effect of using high-temperature phase change materials (PCMs) as energy storage systems for bi-modal systems. This is done by investigating the influence of material properties, such as thermal conductivity and specific heat, to better characterise the system.

The description and design strategy of the novel bi-model system is presented in Section 2. Section 3 discusses the optimisation model approach followed by the optimisation results in Section 4. The transient model and analysis of the receiver is described in Section 5 and its results are discussed in Section 6. Finally, the preliminary design of the proposed system and conclusions are provided in Section 7 and 8.

2. System Description and Design Strategy

The integration of the STP and micro-ORC systems allow sub-systems to share on-board components as shown in Fig. 1, by harvesting energy from the STP receiver to co-generate electrical power, and possibly use the additional waste heat for on-board thermal control. The system consists of 1) an optical system; 2) a high-temperature receiver and thermal energy storage (TES) system; 3) an STP system; 4) a micro-ORC system. The process flow diagram of the micro-ORC system is illustrated

Table 1
Summary of the key system requirements [41].

ID	Requirement	Rationale
STP-01	The propulsion system shall provide a minimum ΔV of 1600 m/s.	Based on a conservative ΔV required to complete the following manoeuvres: (1) Earth escape, (2) mid-course correction, (3) Lunar injection burn and 4) orbit maintenance for one year in a low Lunar orbit.
STP-02	The propulsion system shall have a maximum thrust of 40 N.	To minimise the disturbance torque and reduce the loading conditions on the inflatable concentrators during orbit transfer.
STP-03	The propulsion system shall have a maximum thrusting time of 750 s per orbital manoeuvre.	To reduce the time of exposure of the high-temperature propellant to the nozzle as well as not to limit the disturbance angular momentum.
STP-04	The total time for the Earth escape manoeuvre shall be less than 90 days.	To minimise the radiation exposure to the spacecraft and to compete with the lower range of electric propulsion systems such as the SMART-1 mission that took three months to escape Earth.
STP-05	The propulsion system shall use a propellant with a Fire Protection Association (NPFA) 704 health, flammability, and reactivity rating of less than 4.	To minimise the transport, handling, and integration risks of a small satellite with the primary payload on-board the launch vehicle.
SYS-01	The total wet mass of the integrated system shall be no more than 80% of the spacecraft mass.	Due to the low TRL the acceptable total wet mass is allowed to be greater than typical values of 60 to 75%.
POW-01	The electrical power system shall use a working fluid with a Fire Protection Association (NPFA) 704 health, flammability, and reactivity rating of less than 4.	To minimise the transport, handling, and integration risks of a small satellite with the primary payload on-board the launch vehicle.
POW-02	The electrical power system shall be able to operate continuously.	To ensure the spacecraft can operate during eclipse periods.

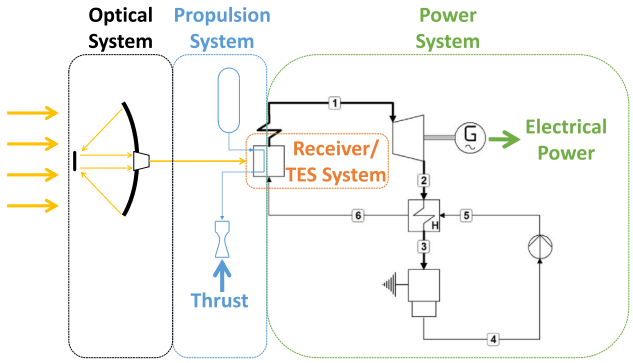

Fig. 1. Schematic of the proposed bi-modal solar thermal system [41].

in Fig. 1. At state 4, the saturated liquid working fluid is compressed to a higher pressure (state 5) by the pump. The regenerator preheats the liquid working fluid to state 6 by using the hot working fluid vapour that exits the turbine (state 2). The receiver vaporises and superheats the working fluid to state 1, which is above the vaporisation temperature.

Fig. 2 provides an overview of the design process used to calculate the mass of the significant components [41]. The figure also highlights the key design parameters that are used in the optimisation process adopted in Section 3.

2.1. Optical system

Design aspects of the optical system include the selection of the concentrator devices and the concentrator-to-receiver coupling method. The concentrator devices can either be mirrors or lenses that are either rigid or inflatable systems that can be fixed or deployable. A parabolic dish is selected as the primary concentrator device because it has higher concentration ratios compared to spherical mirrors and Fresnel mirrors/ lenses and does not suffer from spherical or chromatic aberration [42]. The concentrator-to-receiver coupling can either be directly coupled or optical fibre cables can be used. Fibre optic cable configuration is selected to reduce the pointing accuracy required and decouple the position of the concentrator relative to the receiver. It has been found that by using many smaller mirrors with fibre optic cables instead of one large mirror, the overall system mass can be reduced [43].

A flat plate secondary concentrator is coupled to the primary concentrator to make the optical system more compact by reducing the optical fibre length. It also makes aligning the fibre bundle easier as opposed to a single concentrator configuration. The choice of a flat plate was based on ease of manufacture, simplicity, and compactness at the cost of a small reduction in performance compared to other secondary concentrators such as compound parabolic or refractive concentrators. The proposed optical system does however, decrease the end-to-end power efficiency and has higher complexity due to more components with storage integration challenges.

An important design guideline is to restrict the rim angle of the parabolic dish by the fibre's acceptance angle, which is dictated by the fibre's numerical aperture, to minimise fibre transmission losses. For example, transmission efficiencies are at least 80% when the rim angle is constrained to the fibre acceptance angle [44]. In this design, the acceptance angle of the fibre is 41.3 °.

The mass of the concentrators and support structures can be determined based on areal densities, $\overline{\rho}$, found in [45–47,43,48,17]. The fibre mass is determined by the number of fibres, N_f, multiplied by the length of the fibre, L_f, and the linear density, $\overline{m}_f$, of the fibre. The fibre mass per meter is assumed to be 9.95 g/m [49] and the length is assumed to be twice the primary concentrator diameter. This assumption is based on system integration to accommodate larger concentrators being placed further away from the receiver and avoid restricting the pointing of the concentrator. In this study, inflatable concentrators are used based on their low packaging volume and mass. Therefore an areal density, $\overline{\rho}$, of 1 kg/m^2 [43,48] is used for the concentrator and 1.5 kg/m^2 [17] is used for the support structures. A conservative value for the support structure is used due to the lack of data available on inflatable support structures. The total optical system mass, m_{op}, is made up of the mass of the primary and secondary concentrator indicated by subscripts 1 and 2 respectively, the support structure and the optical fibre mass, all multiplied by the number of optical systems, N_{op}.

The total input power of the optical system, $\dot{Q}_{in}$, can be calculated using,

$$\dot{Q}_{in} = \eta_{op} S N_{op} A_1 \left(1 - b_f\right) \mathrm{BPF} \cos\theta \tag{1}$$

where, S is the solar constant, defined as 1366 W/m^2 at 1 astronomical unit [50], although a conservative value of 1350 W/m^2 is used for this study. A_1, is the area of the primary concentrator, and b_f is the shadow factor defined as the ratio of the area of the primary concentrator shadowed by the secondary concentrator. The optical efficiency, η_{op}, is equal to the combined efficiency of the primary and secondary concentrator and fibres. Concentrator efficiency include reflectivity of the mirrors (90%) and intercept factors (96%), and the fibre efficiency include transmission (90%) and Fresnel efficiency (96.5%) [51]. The bundle packaging factor, BPF, takes into account the packaging efficiency and depends on the cross-sectional area of the fibre, A_f, and bundle, A_b, defined as $\mathrm{BPF} = N_f A_f \; A_b$. Lastly, θ is the solar incidence angle, defined as the angle between the incoming sun's ray and a line normal to the concentrator. For the purpose of this study, the incidence angle is taken as 0 °.

2.2. Receiver/TES storage system

Based on the requirement POW-02, in Table 1, the system requires a thermal energy storage (TES) system. Designing the receiver to also act as a TES system means the number of components can be reduced and thus complexity. This reduction in components will also minimise the mass and volume of the overall system. A latent heat storage system is selected as it can operate at nearly constant temperatures with high energy storage densities and specific energies that are attractive for future planned interplanetary missions and ORC systems. The major challenges with latent storage systems are containment issues such as structural integrity and void formation [17]. The shape of the receiver for the preliminary design is restricted to a cylindrical shape to reduce possible stress concentrations by eliminating corners and accommodating the optical fibres entering the receiver aperture. The physical system is made up of a high-temperature phase change material (PCM) enclosed in a container, as indicated in Fig. 3. The outer surfaces of the container are coated and wrapped in insulation to minimise radiation losses to the space environment. The inner cavity of the container receives the concentrated solar flux. Design parameter of the cylindrical receiver are the outer-to-inner diameter ratio and length-to-outer-diameter ratio. The inner length of the receiver is assumed to be 80% of the outer length. For all simulations, the receiver is assumed to have a 0.25 mm thick Rhenium coating, with a density of 21.03 g/cm^3 density, a 0.5 mm Boron Nitride container that has a density of 1800 kg/m^3 density. From the geometry and density of the PCM, container, and coating the mass of the receiver system can be determined.

A one-dimensional steady-state radial analysis [53] based on first principles is done to determine the thickness of the insulation for a desired outer insulation temperature. The insulation is divided into four layers, and a temperature-dependent thermal conductivity is used to improve the accuracy, using Carbon Bonded Carbon Fibre [54] as the insulation material. The receiver losses, $\dot{Q}_{loss}$ (Eq. 2) are defined as the summation of the radiation loss though the aperture, $\dot{Q}_{rad}$, the absorption losses of the receiver, $\dot{Q}_{abs}$, and the radiation loss through the insulation, $\dot{Q}_{ins}$. From this and the latent heat of the PCM an estimated

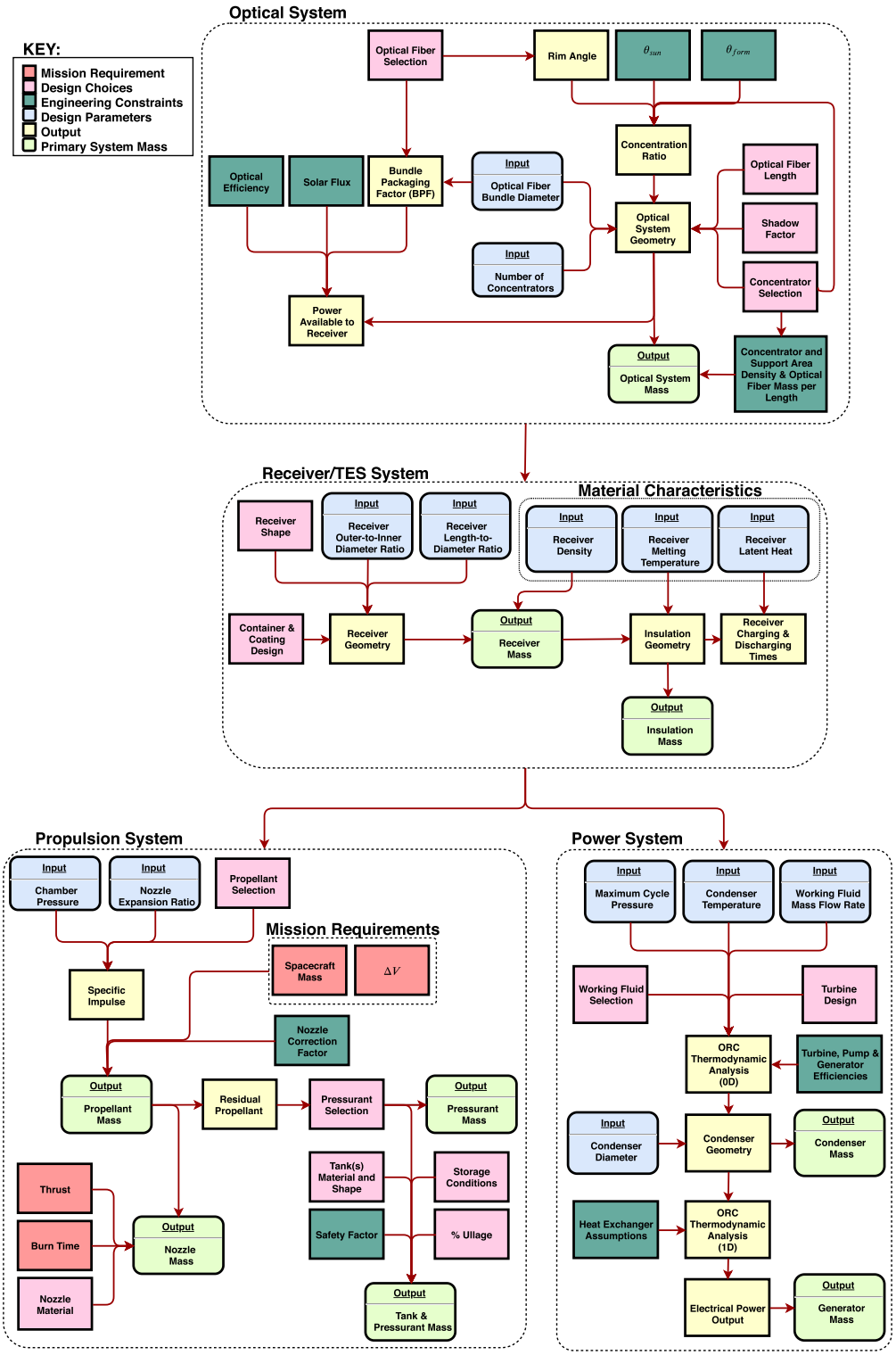

Fig. 2. Simplified flowchart of the integrated solar thermal system design process adopted in this paper [41]. Section 2 provides the detailed information of each step and the relevant equations.

charge, t_{ch}, and discharge time, t_{dis}, can be computed. This is only possible if the energy available per orbit is greater than the energy required by the propulsion system during each burn, the energy required by the ORC system and the energy associated with losses. Fully charging the TES is assumed to incorporate only the latent heat storage due to the preliminary nature of this study, and the available input and output powers are assumed to be steady-state values. The energy fluxes are described by

$$\dot{Q}_{loss} = \dot{Q}_{ins} + \dot{Q}_{rad} + \dot{Q}_{abs}, \tag{2}$$

$$\dot{Q}_{rad} = \varepsilon \sigma A_{ap} \left(T_{rec}^4 - T_{space}^4 \right), \tag{3}$$

$$\dot{Q}_{abs} = \left[1 - \frac{\alpha_{rec}}{\alpha_{rec} + (1 - \alpha_{rec}) A_{ap} / A_{in}} \right] \dot{Q}_{in}, \tag{4}$$

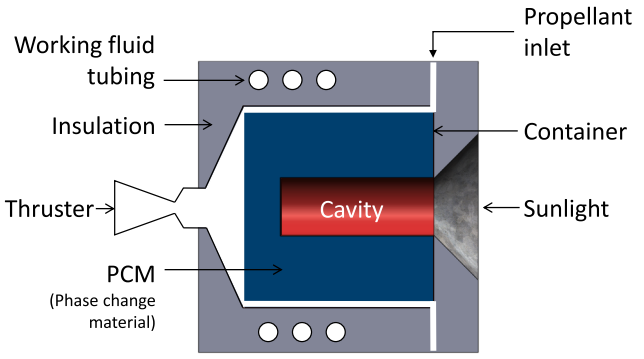

Fig. 3. Schematic representation of the receiver with straight channel propellant tube configuration and one thruster [52].

$$\dot{Q}_{ins} = \varepsilon\sigma A_{ins}\left(T^4_{ins,o} - T^4_{space}\right), \tag{5}$$

where α_{rec} is the absorptivity of the receiver, ε is the emissivity of the receiver, σ is the Stefan–Boltzmann constant, A_{ap} is the cross-sectional area of the aperture, A_{in} is the inner surface of the receiver, and A_{ins} is the surface area of the insulation. $T_{ins,o}, T_{rec}, T_{space}$ correspond to the outer insulation layer, the receiver, and the environmental temperatures respectively. The remaining variables are

$$t_{ch} = \frac{m_{pcm}L}{\dot{Q}_{in} - \dot{Q}_{orc} - \dot{Q}_{loss}}, \tag{6}$$

$$t_{dis} = \frac{m_{pcm}L}{\dot{Q}_{orc} + \dot{Q}_{loss}}, \text{if} \dot{Q}_{in}t_{daylight} > \dot{Q}_{orc}t_{orbit} + \dot{Q}_{prop}t_{burn} + \dot{Q}_{loss}t_{orbit}, \tag{7}$$

where m_{pcm} is the mass of the PCM, L is the latent heat of the PCM, and $\dot{Q}_{orc}$ is the power required for the ORC system.

A key design challenge is the different operating temperatures of the ORC and the STP system. Organic fluids are restricted by their thermal stability limit at around 300 to 400 °C [55–57] and STP desire temperatures above 1000 K to achieve high specific impulse values. This temperature limit affects the design of the system and thus results in the working fluid tubing being embedded inside the insulation layer if the melting temperature of the receiver material exceeds the thermal limit of the working fluid.

2.3. Power system

The on-board electrical power is generated by using an ORC system made up of a working fluid, condenser, generator, regenerator, turbine, and tubing.

2.3.1. Working fluid selection

The ORC operates by vaporising the working fluid being passed through a coiled tubing inside the insulation of the receiver. Based on a pre-screening study conducted on 79 potential organic working fluids [58] and a working fluid optimisation [59], Toluene is selected as the working fluid. Toluene meets the POW-01 requirement and is the optimal fluid in terms of system volume minimisation.

The preliminary design of the micro-ORC system has been carried out using a Matlab code based on the work of [60]. Fluid thermophysical properties are determined by integrating the code with the software library Fluidprop [61]. The thermodynamic cycle analysis procedure used in this model can be found in [62,63]. The condenser is a significant component in terms of mass for a micro-ORC system [59] and therefore designed in more detail. After the evaluation of the design condenser and the pressure drop calculated, the ORC thermodynamic analysis is re-evaluated including the pressure drops of all the heat exchangers. The pressure drop for both sides of the regenerator, as well as evaporator, is assumed to be 1% based on the works of [59].

2.3.2. Condenser

Heat is radiated to space using a condenser designed with two thin flat sheets of aluminium on the top and bottom coupled to several circular channels. The conductor has a honeycomb support structure in-between, as depicted in Fig. 4. The length of the circular channels are discretised into smaller segments, and the heat transfer and pressure loss are calculated for each length.

To describe the two-phase heat transfer and pressure drop of the condensing section of the channels, the universal approach developed by [64,65] has been used due to its broad range of applicability. Reference [41] describes the implementation of the condenser model. The effects of gravity are neglected, which is acceptable during coasting parts of the mission. The area of the radiator, A_{rad}, is determined based on the heat-pipe analysis described by [66] using

$$\dot{Q} = \varepsilon\sigma\eta_e A_{rad} T_B^4 \tag{8}$$

where $\dot{Q}$ is the total radiation power of the condenser-radiator system, ε is the emissivity of the radiator, σ is the Stefan–Boltzmann constant, and T_B is the temperature at the fin base. The fin effectiveness, η_e, is a function of the dimensionless temperature, θ^*, and radiation parameter, ζ.

$$\eta_e = \begin{cases} \left(1 - 1.125\xi + 1.60\xi^2\right)\left(1 - \theta^{*4}\right), 0.01 \leqslant \xi \leqslant 0.2 \\ \left(-0.405\log\xi + 0.532\right)\left(1 - \theta^{*4}\right), 0.2 \leqslant \xi \leqslant 2.0 \end{cases} \tag{9}$$

$$\xi = \frac{\sigma L^2 T_B^3(\varepsilon_1 + \varepsilon_2)}{kt} \tag{10}$$

$$\theta^* = \frac{T_s}{T_B} \tag{11}$$

where, L is the half-length between the channels, k is the thermal conductivity of the fin, t is the thickness of the fin, and T_s is the radiative sink temperature. The emittance of the top and bottom side of the radiator is indicated as ε_1 and ε_2 respectively,

The mass the condenser, m_{cd}, is the summation of the mass of the working fluid inside the channels (taken as liquid to be conservative), m_{wf}, the channels, m_{ch}, the aluminium fins, m_{fin}, the honeycomb core, m_{core}, an adhesive layer, m_{ad}, and an optical solar reflector (OSR) layer, m_{OSR}. The support structure and deployment mechanisms have not been considered for simplicity. However, an additional margin of 20% has been included in the total system mass to account for these unknowns.

$$m_{cd} = m_{wf} + m_{ch} + m_{fin} + m_{core} + m_{ad} + m_{OSR} \tag{12}$$

2.3.3. Generator

Based on a micro-generator survey [59] a linear relationship between the generator mass, m_{gen} and electrical power, $\dot{W}_{net}$ was derived, where the coefficients c_1 and c_2 are defined as 1.8 kg/kW and 2.718 kg,

$$m_{gen} = c_1\dot{W}_{net} + c_2. \tag{13}$$

2.3.4. Additional components

The regenerator, turbine, and tubing between the ORC components are the remaining components of the micro-ORC system. The regenerator improves the efficiency of the cycle. A cross-flow platefin heat

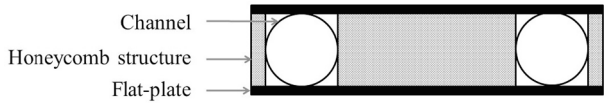

Fig. 4. Cross-sectional view of a portion of the condenser showing 2 channels, the honeycomb structure and the flat-plate fins [52].

exchanger with rectangular channels is chosen due to its lightweight, compactness, and ability to operate at high temperatures. A radial inflow turbine is selected due to its compactness and potential high power density. At these small-scales the real challenge to attain acceptable turbine efficiency levels is the proper design and manufacturing of the tip gap to reduce leakage flow. To account for the decay in efficiency due to the small-scale of the turbine design a total-to-static efficiency of 65% is used. Although, this may be an optimistic value for the lower power capacity designs as previous work demonstrated that a conservative efficiency of 57% for a 200 W micro-turbine design [52] is realistically attainable. In addition, there is research being conducted on improving the performance of small-scale ORC systems [67]. The regenerator, turbine, and tubing mass are included as part of the 20% margin due to their low contribution to the total mass [52].

2.4. Propulsion system

The propulsion system is made up of the propellant, the feed system, and the nozzle.

2.4.1. Propellant selection

Existing theoretical and experimental STP systems have used propellants such as ammonia, helium, hydrazine, hydrogen, nitrogen, and water. Hydrazine is excluded as it does not conform to the STP-05 requirement. Another aspect that needs to be considered is the storability of the propellant for the entire mission duration. Thus, high performing propellants such as hydrogen and helium are excluded because although they have a high specific impulse, they have low storage density. Furthermore hydrogen suffers from boil-off and therefore not suitable for long-term storage. Nitrogen is suitable to test STP systems but is discarded due to large storage requirements and poor specific impulse.

From the remaining propellants, ammonia has attractive qualities such as self-pressurising capabilities and higher specific impulse values than water. However, water is chosen due to its higher storage density, moderate performance (10% reduction compared to ammonia), and safer attributes regarding health flammability and reactivity. Challenges with using water as a propellant include potential freezing, thruster corrosion, and the need for a pressurant system.

The specific impulse, I_{sp}, and the propellant mass, m_p, are determined from the mission requirements, ΔV, and spacecraft mass, $m_{s/c}$, and the nozzle correction factor, λ, expansion ratio, $\in$, chamber pressure, P_{ch}, and the temperature of the propellant (taken as T_{melt}). The nozzle expansion ratio, chamber pressure and propellant temperature are design inputs and are free to vary within a specified range. For simplicity of manufacture, a short conical nozzle is assumed with a nozzle correction factor of 96% [68].

$$I_{sp} = \frac{c^* \gamma}{g} \sqrt{\left(\frac{2}{\gamma - 1}\right)\left(\frac{2}{\gamma + 1}\right)^{\frac{(\gamma+1)}{(\gamma-1)}} \left[1 - \left(\frac{P_e}{P_{ch}}\right)^{\frac{(\gamma-1)}{\gamma}}\right]} \tag{14}$$

where c^* is the characteristic velocity, g is the gravitational acceleration (9.81 m/s^2), γ is the propellant's ratio of specific heats determined at the maximum propellant temperature, and P_e is the exit pressure of the nozzle

$$m_p = m_{s/c}\left(1 - e^{\left(\frac{-\Delta V}{\lambda g I_{sp}}\right)}\right). \tag{15}$$

2.4.2. Feed system

The feed system consists of the propellant tanks, pressurisation system, flow lines and valves. Design choices for the tanks include the selection of the material (composite wrapped, aluminium alloys or titanium), the shape of the tank (cylindrical with hemispherical endcaps or spherical) and the number of tanks. These choices affect the mass and packaging volume of the system. The fluid inside the tanks is assumed to undergo isentropic expansions due to the relative long burn per manoeuvre. Using water requires a pressurant system to be included in the design. In this case, a regulated pressure-fed system is selected as the pressurisation system ensures constant operating pressure and therefore thrust, assuming a constant propellant temperature. All the tanks are assumed to be manufactured out of Titanium alloy, Ti-6Al-4 V [69]. A single spherical pressurant and propellant tank is assumed. To account for pressure losses in the system such as orifices, regulators, and bends and to prevent backflow, the propellant tank final pressure is assumed to be twice the chamber pressure. The maximum expected operating pressure (MEOP) is assumed to be 15% more than the design pressure, and the burst pressure is 1.5 times the MEOP. To determine the thickness, t, of the tanks (Eq. 16) a safety factor, SF, of 2.4 is used. The safety factor is a product of a 1.2 safety factor over the yield strength, σ_y, and a 2.0 safety factor to account for higher loads and vibration expected during launch [70]. The thickness of the tank wall, t, is

$$t = \frac{(SF)Pr}{(C)\sigma_y} \tag{16}$$

where C is the shape constant and is equal to 1 if the tank is cylindrical and 2 if spherical. P is the burst pressure, and r is the inner radius of the tank. A minimum wall thickness of 0.5 mm is assumed [71] due to manufacturing capabilities. For this paper, the mass of the flow lines and valves are not included and assumed to be part of the margin.

2.4.3. Nozzle

A simplified nozzle design was used to calculate the mass of the nozzle in relation to increasing expansion ratio. For this design, the divergence angle and convergence angle are assumed to be 15° and 60 °. The outer diameter, length, and mass of the nozzle are functions of the chamber pressure, burn time and expansion ratio. It should be noted that in reality the design should be modified to consider specific mission constraints such as vibration loads.

2.5. Model validation

Validation of the mass calculations of the condenser, receiver and optical system have been conducted. The concentrator is one of the largest components of the system, and therefore it is important to ensure the sizing is properly modelled. Table 2 presents the results of this study against the works of [6,72] and falls within an acceptable range. The large deviation of 17% for the stowed volume is due to the limited information of the 0.5 m dish design from [72] and the rigid volume in this study is computed as a cylinder using the concentrator diameter and focal length. The work of [17] has been used to validate the sizing of the phase change receiver model. The results fall within a 2% difference. The discrepancy is possibly due to a difference in densities used. The condenser validation assumed a two-sided flat aluminium heat pipe radiator that operates at 21 °C with a sink temperature of −87 °C, the heat pipe mass per meter is 0.11 kg/m, and 1000 W is required to be radiated. The analysis was conducted for a range of fin thickness values (0.18 to 0.5 mm) and pipe spacings (0.1 to 0.3 cm) with the results showing an average difference less than 3%. All models, except for the volume of the optical system, are within the acceptable threshold of 5%. The large 17% deviation of the volume concentrator model is still acceptable as mass is the important parameter considered, which meets the 5% threshold. The storage volume of the concentrator is linked to the concentrator's areal density taken from literature which is an acceptable conservative approach. The mass of the propulsion system components and propellant are computed with commonly used equations in preliminary design phase [73] and therefore deemed suitable for this

Table 2
Model validation results.

System	Parameter	Unit	Reference Value	Reference	This Study	Difference [%]
Receiver						
	PCM Mass	[kg]	66.8	[17]	67.3	0.7
	Container Mass	[kg]	9.4	[17]	9.3	1.1
	Coating Mass	[kg]	62.6	[17]	52.4	0.4
	Total Mass	[kg]	128.8	[17]	129	0.2
Optical						
	Focal Length	[mm]	33.7	[6]	33.8	0.3
	Mass	[kg]	15	[6]	14.78	1.5
	Rigid Volume	[m^3]	0.05	[72]	0.0593	17
Condenser						
	Average Area	[m^2]	5.24	[66]	5.16	1.4
	Average Mass	[kg]	3.76	[66]	3.67	2.9

analysis.

3. Optimisation model approach

The objective of this work is to optimise the bi-modal system that could lead to a more competitive design over conventional systems. In this case, the mission parameter constants are the ΔV required for the mission (1.6 km/s) [74,40], the initial orbit parameters, taken as a Geostationary Transfer Orbit (GTO), and the gross mass of the spacecraft.

The goal is to minimise the overall wet mass fraction, β, defined as the mass of the bi-modal system, m_{sys}, over the total spacecraft mass, $m_{s/c}$,

$$\beta = \frac{m_{sys}}{m_{s/c}}. \tag{17}$$

Reducing the overall wet mass fraction leads to a better performing design by minimising the mass of propellant on-board the spacecraft and improving the ORC efficiency by minimising the concentrator size. The wet system mass is made up of the mass of the optical system, the receiver, the insulation, the propellant, the propellant tank, pressurant, and pressurant tank, the nozzle, and the condenser. A 20% margin on the wet system mass is included to account for any unknowns and additional components such as the regenerator. The amount of time required to fully charge and discharge the PCM which acts as the TES system, assuming steady-state input and output power operation, is constrained to a maximum of 536 min and 104 min respectively based on daylight and eclipse periods of a GTO described by [75]. This restriction is to ensure the system operates during eclipse periods at the initial orbit.

The optimisation problem is solved using a single-objective genetic algorithm (GA) using the code presented in [76]. Fig. 5 illustrates the optimisation process. GAs are commonly used in ORC and heat exchanger optimisation studies due to their robustness. However, they require higher computational time [77,78]. The objective function, $F(x)$, consists of the overall wet mass fraction and a penalty term, $P(x)$,

$$\underbrace{F(x)}_{\min} = \beta\left(x\right) + P\left(x\right). \tag{18}$$

A penalty is calculated if the fluid velocity in the condenser is outside the boundary for liquid, gas, or two-phase flow [79]. To ensure the entire design space is investigated the population size and the maximum number of generations is set to 130 and 400. The termination criteria are set as either a convergence criterion of 10^{-10} or the maximum number of generations. An initial mutation rate of 0.02 and a crossover probability of 0.7 are also used. Five spacecraft were investigated with a gross mass of 100, 200, 300, 400, and 500 kg respectively with an electrical power requirement of at least 1 W/kg. The chromosome structure is made up of thirteen design parameters, indicated in Fig. 2, that describe the bi-modal system and mass of the major components.

4. Optimisation results

Fig. 6 provides the final optimisation solutions of the wet mass fraction. The corresponding design parameters are given in Table 4. The results show that there is a small variation in wet mass fraction with respect to satellite gross mass. For a spacecraft mass of 200 kg or less, the system requirement SYS-01 is not met. The spacecraft mass of 400 kg and 500 kg are the more suited for the GTO to Lunar mission as they have a mass fraction close to 75% which could compete with conventional systems [80]. Using tanks that are composed of a combination of titanium and composite materials could further reduce the mass fraction of the existing design to make it more competitive. The larger designs also result in fewer concentrators and therefore could reduce complexity by employing simpler deployment and tracking systems. The use of a constant total-to-static turbine efficiency for all the five mini-satellites results in the mass fraction for the smaller power capacity designs to be higher than in reality. This provides more confidence on the suitability of the proposed bi-modal design concept for the higher power capacity designs. Moreover, Table 3 indicates that for satellites less than 300 kg the rotor blade height is below the minimum acceptable limit of 0.2 mm that is possible with current manufacturing limitations [59]. The results also show that the higher mass satellites exhibit slower rotational speeds and better shared specific power which are more beneficial in terms of technical feasibility.

The PCM design parameters results in Table 4 show a melting temperature, density, and latent heat range of 1500 to 2000 K, 1800 to 3000 kg/m^3, and 4600 to 5000 kJ/kg respectively. Silicon and Boron are existing PCM that best fit these ranges. However, Silicon does not meet the latent heat range and Boron slightly exceeds the melting temperature range, refer to Table 5 [17,81,6,82–84]. These materials meet the future planned interplanetary specific energy target of greater than 250 Wh/kg. Table 5 highlights that Silicon is more appropriate than Boron based on a trade-off of material properties, availability, and cost and will be used as PCM for the following dynamic investigation.

The propellant mass accounts for between 40% and 50% of the total mass, as depicted in Table 6. The normalised propellant mass is dependent on the melting temperature of the optimal solution. The 200 kg satellite has the lowest melting temperature and, therefore, results in highest propellant mass fraction. The next highest mass components are the concentrator and insulation contributing up to 8% of the total mass. The tank system (including pressurant gas), condenser, nozzle, and receiver account for approximately 3.8%, 1.7%, 1.7% and 1.3% of the total mass regardless of the spacecraft size. The generator normalised mass decreases with increasing spacecraft size due to the empirical equation used.

5. Bi-modal system dynamic model approach and validation

The dynamic model of the receiver is executed using MATLAB/

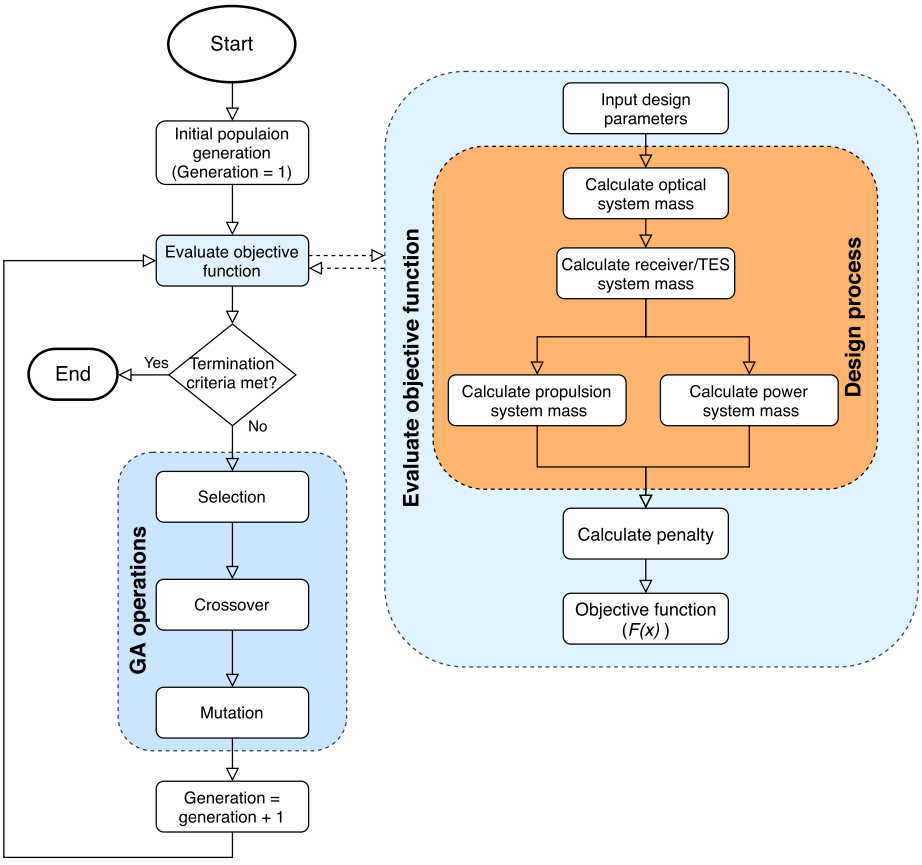

Fig. 5. Flowchart illustrating the optimisation process. Section 2 discusses the design strategy used to evaluate the objective function.

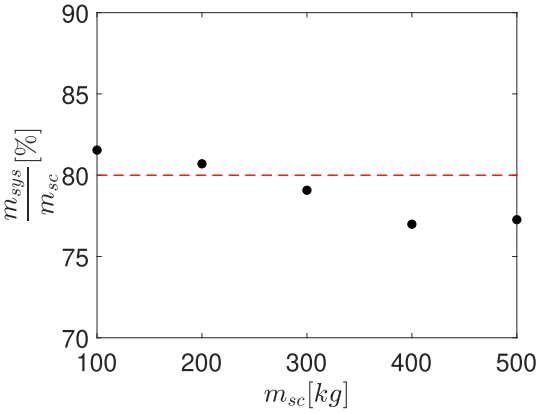

Fig. 6. Final optimal solution of the wet mass fraction of the propulsion and power system for the five satellites. The dashed line represents the upper limit of wet mass fraction as per requirement SYS-01. [41].

Simulink for ease of integration with the models developed in Section 2. The enthalpy method introduced by [85] is commonly used to investigate the phase change behaviour of the material [86]. The PCM can be divided into three regions a solid, a liquid, and a mushy zone (containing both liquid and solid phases). Therefore, the method is dependent on the liquid fraction, f, which denotes the ratio of liquid to the total mass of the domain. The solid and liquid regions are defined as $f = 0$ and $f = 1$ respectively and the mushy zone is $0 < f < 1$. The conservation of the total specific energy, e, for the system reads

$$\frac{de}{dt} = \dot{e}_{in} - \dot{e}_{out}. \tag{19}$$

The total specific energy is a function of the sensible and latent heat,

$$e = \left(e_{s,ref} + \int_{T_{ref}}^{T} c dT \right) + fL \tag{20}$$

where, c is the specific heat capacity, T_{ref} is the reference temperature, T is the current temperature, $E_{s,ref}$ is the reference sensible specific energy at the reference temperature, and L is the latent heat of fusion.

Table 3
Micro-turbine and ORC results of the optimisation study.

S/C Mass [kg]	Rotor blade height [mm]	Rotor diameter [mm]	Rotational speed [rpm]	Thermal efficiency [%]	Electrical power output [W]	Shared specific power* [W/kg]
100	0.11	4.1	1 381 600	21.37	106.75	9.4
200	0.19	5.0	1 020 400	18.69	216.10	11.1
300	0.33	6.9	693 040	16.65	332.88	12.1
400	0.27	7.1	715 480	18.65	418.08	12.1
500	0.32	8.8	597 860	19.13	540.49	12.6

* **Shared specific power is defined as output electrical power over the mass of the ORC components only. Mass of the ORC components is equal to the sum of the condenser, generator and half of the margin mass. Other half allocated to the propulsion system.**

Table 4
Final optimised design parameters for each mini-satellite investigated [41].

S/C mass [kg]	D_b [mm]	D_o/D_i	L/D	ε	P_c [bar]	T_{melt} [K]	ρ [kg/m^3]	L [kJ/kg]	$\dot{m}$ [g/s]	P_{max} [bar]	T_{cd} [K]	D_{cd} [mm]	N_{conc}
100	3	3.76	1.87	226	4.89	1550	2946	4839	1.14	31.78	115	0.20	19
200	5	2.80	2.77	193	4.76	1501	2768	4970	2.95	33.9	142	0.22	16
300	7	3.30	1.94	172	4.21	1851	2462	4744	5.05	21.04	144	0.62	12
400	7	3.64	1.68	221	4.57	1849	1844	4938	5.63	31.15	139	0.52	14
500 (*baseline**)	14	3.38	0.97	166	4.37	1964	2785	4617	6.78	26.69	129	0.368	5

* Configuration used in the transient analyses in Section 5.

Table 5
Comparison of PCM candidates [17,81,6,82–84].

PCM	Melting temperature	Latent heat	Specific energy	Thermal conductivity	Abundance	Cost
Silicon	1410 °C (Orange)	1800 kJ/kg (Orange)	496 Wh/kg (Green)	25-56 W/mK (Green)	High (Green)	$ 1.7/kg (Green)
Boron	2076 °C (Green)	4650 kJ/kg (Green)	1278 Wh/kg (Blue)	<30 W/mK (Orange)	Rare (Red)	$ 5/g (Red)

Blue: Exceeds requirements, Green: Meets requirements, Orange: Correctable deficiencies, Red: Unacceptable

Table 6
Mass budget relative to gross mass of the spacecraft for each mini-satellite.

S/C Mass [kg]	Optical system	Receiver	Insulation	Condenser	Generator	Nozzle	Tank systems	Pressurant	Propellant	Margin	Available
100	4.5%	1.1%	4.9%	1.7%	2.9%	1.3%	3.2%	0.6%	47.8%	13.6%	14.3%
200	5.7%	1.1%	3.9%	1.4%	1.5%	1.2%	3.2%	0.6%	48.6%	13.5%	19.0%
300	6.1%	1.3%	6.8%	1.5%	1.1%	1.3%	2.6%	0.5%	44.8%	13.2%	21.4%
400	5.3%	1.0%	6.1%	1.3%	0.9%	1.7%	2.8%	0.5%	44.5%	12.8%	24.5%
500	7.8%	1.0%	5.2%	1.4%	0.7%	1.3%	2.6%	0.5%	43.7%	12.9%	24.4%

The mathematical representation of the receiver is based on the following assumptions:

1. only radiative losses between the receiver and the external environment are considered, as the system is operated in vacuum conditions,
2. the volume variation during the phase change process is ignored,
3. the effects of natural convention and Marangoni convection within the PCM is negligible,
4. the PCM thermophysical properties are different for the liquid and solid phases (Table 7),
5. in the mushy zone the PCM thermophysical properties are assumed to vary linearly,
6. the PCM is assumed to behave ideally such that property degradation and supercooling effects are not accounted, and
7. heat conduction in the longitudinal direction is negligible.

Table 7
Solid and liquid thermophysical properties of Silicon.

Thermophysical property	Units	Value	Reference
Solid density	kg/m^3	2520	[87,83]
Liquid density	kg/m^3	2520	[87,83]
Solid specific heat	J/kgK	Shomate Equation†	[88]
Liquid specific heat	J/kgK	1040	[87,83,84]
Solid thermal conductivity	W/mK	polynomial function‡	[82]
Liquid thermal conductivity	W/mK	56	[89]
Solidus temperature	K	1684	[83,84]
Liquidus temperature	K	1686	[83,84]
Latent heat	kJ/kg	1800	[87,83,84]

† where the Shomate coefficients are A = 22.81719, B = 3.89951, C = −0.082885, D = 0.042111,
and E = −0.354063, for 298⩽T⩽1684

‡ $k_{pcm,s}(T) = 1.0807 \times 10^{-10}T^4 - 5.2458 \times 10^{-7}T^3 + 9.5562 \times 10^{-4}T^2 - 8.0147 \times 10^{-1}T + 295.74$
for 373⩽T⩽1684

However, in reality, some of the above assumptions do not hold. Nevertheless, the following justifications are provided to show that the changes generated by these effects are either negligible or conservative, and the benefit of simplifying the modelling outweighs the errors.

The work of [87] states that Assumption 3 is plausible if the liquid Silicon has a small temperature gradient because the corresponding density change is minimal. Besides, by modelling the natural convection within the PCM, the heat transfer would be improved; therefore, this assumption represents a more conservative heat transfer estimation for the PCM [90]. Reference [91] states that for PCM under microgravity conditions, natural convection disappears and Marangoni convection, caused by surface tension, become apparent in the presence of a void in the cavity. However, Marangoni convection is an order of magnitude smaller than natural convection. Therefore Assumption 3 remains acceptable.

Constant liquid PCM thermophysical properties are assumed as they are relatively constant during the expected operational temperature range of the receiver (Assumption 4). It is also assumed that the receiver will operate close to the melting temperature during nominal operation by varying the incidence angle between the Sun and the concentrator dish. On the other hand, solid thermophysical properties are temperature-dependent and defined in Table 7.

Assumption 7 is only valid for short characteristic lengths [92,6] that result in Biot numbers significantly less than one. The effective Biot number, Bi_e, (Eq. 21) indicates the significance of internal conduction within the receiver material relative to radiative cooling [6].

$$Bi_e = \frac{\varepsilon\sigma\left(T_b^2 + T_a^2\right)(T_b + T_a)L}{k} \tag{21}$$

where, ε is the material's emissivity, L is the characteristic length, and k is the materials thermal conductivity. The temperature of the body, T_b, is taken as the melting temperature of the PCM, and T_a is the ambient temperature.

Table 8 illustrates that the effective Biot number for the 500 kg optimal solution case using Silicon is between 0.13 and 0.36 at its

melting temperature. This falls outside the model validity, which is Biot numbers less than 0.1 [105]. However, modelling the PCM as a lumped-capacity node instead of using finite difference conduction models results in an overestimation of the surface temperature of the PCM which will result in higher radiation heat transfer to its surroundings and therefore have a lower peak body temperature [6]. Thus, for the initial characterisation of the PCM of the bi-modal system to determine the system's feasibility, neglecting the longitudinal temperature variation is acceptable. However, caution is noted on future designs to include a finite-difference model in the longitudinal direction.

To investigate the radial distribution of the PCM, three models were developed, a first-order (2R1C), a second-order (4R2C), and a third-order (6R3C) model, as depicted in Fig. 7. These models are made up of 2, 4 and 6 variable thermal resistances and 1, 2, and 3 variable thermal capacitances respectively. The parameters are determined based on the physical properties and temperature of the material. The cylindrical insulation is sub-divided into sub-cylinders that consists of one capacitance and two resistances. Thermal conductivity, k, of each thermal resistor is a function of temperature corresponding to the node left of the resistor in Fig. 7. This premise provides a more conservative value due to the higher reference temperature and therefore, larger thermal conductivity for the resistor. Two coefficients, α and β are derived to describe the radial positing of the capacitance and resistance, as shown in Fig. 7. α_i is defined as the ratio of the capacitance at the i-th node to the total capacitance. The ratio of the resistance at node i over the total resistance is denoted as β_i. The insulation model has a large radial temperature distribution from the inner surface near the PCM and outer surface which radiates to the environment, therefore, a third-order model was used for the insulation.

The differential heat balance equations of the PCM are defined as Eq. 22–25 according to the first and second law of thermodynamics for a generic first-order ($j = 1$), second-order ($j = 2$) and third-order ($j = 3$) models. Fig. 8 presents the flowchart of the transient process to determine the heat transfer and temperature of each node.

$$C_{p,1\,(j=1)}\frac{dT_{p,1}(t)}{dt} = \frac{T_{c,1}(t) - T_{p,1}(t)}{R_{c1,out} + R_{p,1}} - \frac{T_{p,1}(t) - T_{c,2}(t)}{R_{p,2} + R_{c2,in}}, \text{or} \tag{22}$$

$$C_{p,1\,(j=2=3)}\frac{dT_{p,1}(t)}{dt} = \frac{T_{c,1}(t) - T_{p,1}(t)}{R_{c1,out} + R_{p,1}} - \frac{T_{p,1}(t) - T_{p,2}(t)}{R_{p,2} + R_{p,3}} \tag{23}$$

$$C_{p,2\,(j=2,3)}\frac{dT_{p,2}(t)}{dt} = \frac{T_{p,1}(t) - T_{p,2}(t)}{R_{p,2} + R_{p,3}} - \frac{T_{p,2}(t) - (j-2)T_{p,3}(t) - (3-j)T_{c,2}(t)}{R_{p,4} + (j-2)R_{p,5} + (3-j)R_{c2,in}} \tag{24}$$

$$C_{p,3\,(j=3)}\frac{dT_{p,3}(t)}{dt} = \frac{T_{p,2}(t) - T_{p,3}(t)}{R_{p,4} + R_{p,5}} - \frac{T_{p,3}(t) - T_{c,2}(t)}{R_{p,6} + R_{c2,in}} \tag{25}$$

where, T, is the temperature of the specified node according to Fig. 7, R, is the thermal resistance and, C, is the heat capacity, defined as a function of its coinciding temperature,

$$C_{p,i} = \alpha_i C_{tot}(T_i) \tag{26}$$

Table 8
Biot numbers for the 200 kg and 500 kg optimal solutions.

Receiver Design (Characteristic length)	200 kg case (0.220 m)	500 kg case (0.129 m)
Silicon (k = 20 W/mK)*	0.62	0.36
Silicon (k = 56 W/mK)**	0.22	0.13

Ambient temperature taken as 300 K to obtain worst-case values.
The emissivity of molten Silicon is 0.17 [93,94].
* Solid at melting temperature.
** Liquid at melting temperature.

$$C_{tot}\left(T_i\right) = \frac{1}{4}\pi\left(d_{p,out}^2 - d_{p,in}^2\right)L_p\rho_p c(T_i) \tag{27}$$

where, $i = 1,2,3$ and corresponds to the node of interest, $d_{p,in}$ and $d_{p,out}$ are the inner and outer diameter of the PCM, and L_p, ρ_p, and c are the latent heat, density and specific heat of the PCM.

$$R_{p,(2i-1)} = \alpha_i\beta_i R_{tot}\left(T_i\right) \tag{28}$$

$$R_{p,(2i)} = \alpha_i(1-\beta_i)R_{tot}\left(T_i\right) \tag{29}$$

$$R_{tot}\left(T_i\right) = \frac{1}{2\pi k_p(T_i)L_p}\ln\frac{d_{p,out}}{d_{p,in}}. \tag{30}$$

The insulation model has a large radial temperature distribution from the inner surface near the PCM and outer surface which radiates to the environment. Therefore, a third-order model was used for the insulation to capture the change in temperature dependent properties, such as thermal conductivity. Additionally, higher degree in refinement is necessary to determine the placement of the working fluid. The differential heat balance equations for the insulation sub-cylinders can similarly be defined by replacing the thermal resistance $R_{c1,out}, R_p$, and $R_{c2,in}$ with $R_{c2,out}$, R_{ins}, and R_{rad} and changing the temperature nodes from $T_{c1,out}, T_p$, and $R_{c2,in}$ to T_{c2}, T_{ins}, and T_{space} respectively.

5.1. Receiver validation and verification

The first-order PCM model developed is validated against experimental data and a two-dimensional numerical model for a low-temperature melting case [92] and a high-temperature solidification case [95]. For these validation cases, convection heat transfer was included. The results of the two cases are shown in Fig. 9a and b. Fig. 9c shows the maximum percentage error is 19% and 12% against the experimental data and numerical results respectively, for the melting case study and 3% and 4% against the experimental data and numerical results, for the solidification case. The results illustrate that 2RC1 model can adequately capture the heating and cooling dynamics of a PCM. Note, a constant temperature during the melting/solidification of the PCM for the validation simulation was assumed for the 2RC1 model.

Each of the three models (2R1C, 4R2C, and 6R3C) were run using the 500 kg optimal solution receiver geometry to determine the effect of varying the number of nodes distributed radially in the PCM. Table 9 provides the maximum absolute relative percentage difference with respect to the average[1] obtained for various nodes over one orbit for each model. Higher-order models have smaller percentage differences, although, the most considerable maximum absolute relative percentage difference is only 5.5% when comparing the 2R1C with the 6R2C model. The time step for the 6R3C model had to be reduced to 0.002 s, to prevent instabilities, which resulted in a significant increase in the simulation running time. Therefore, as a trade-off between computational resources and accuracy in describing the phase change composition inside the receiver, the 4R2C model is used for the following investigations. For precise determination of the liquid–solid interface during the phase change process finer discretisation radially as well as longitudinally is needed; however, for this study, the overall behaviour of the receiver is of interest.

Increasing the 4R2C model time step to 0.01 s decreases the simulation time by a factor of 3.9 at the expense of a maximum relative percentage difference of 2.2%, 0.3%, 1.1%, 0.3%, and 0.3% for $T_{c,1}, T_{p,1}$,

[1] An example of the maximum absolute relative percentage difference between the 6R3C and 2R1C model: $|RD_{\max}(T_{c,1})| = max\left(\frac{|T_{c,1}(t)_{6R3C} - T_{c,1}(t)_{2R1C}|}{0.5[T_{c,1}(t)_{6R3C} + T_{c,1}(t)_{2R1C}]}100\right)$.

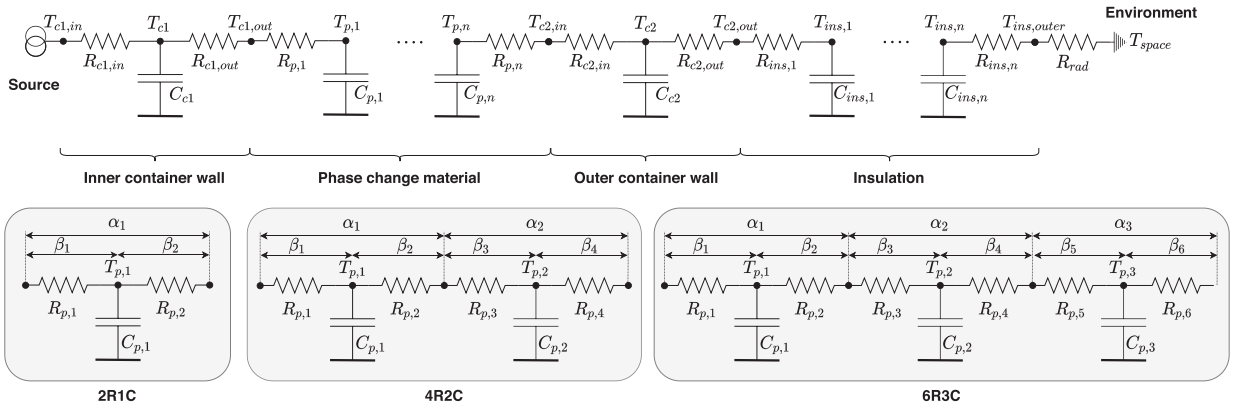

Fig. 7. Thermal nodal network of the receiver.

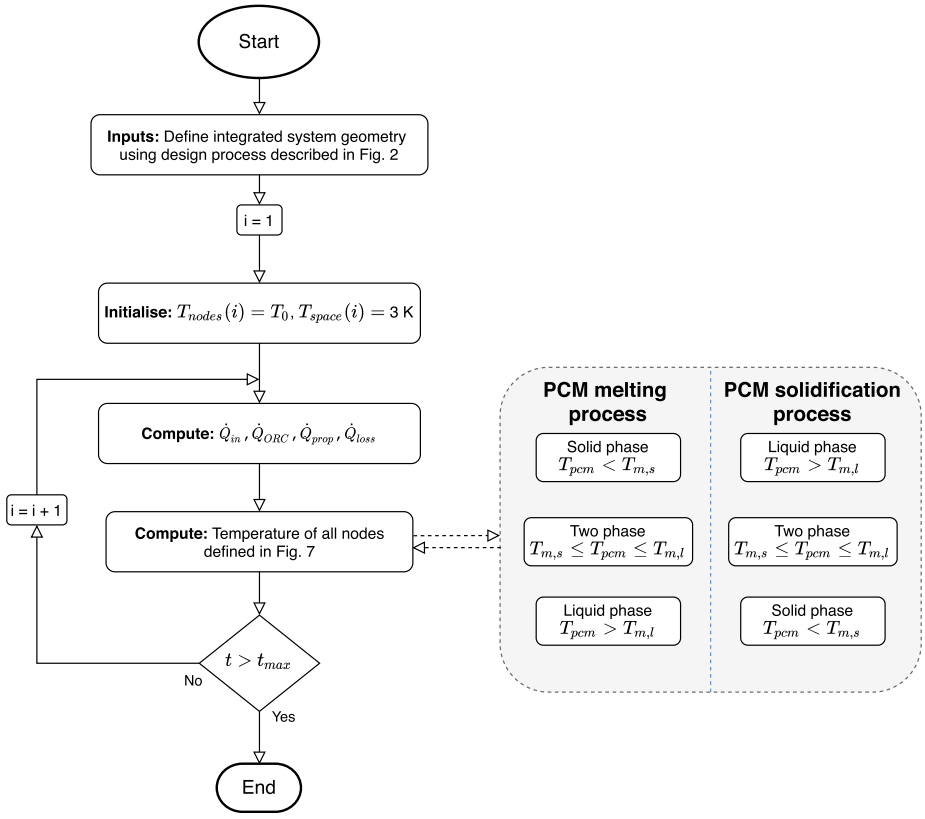

Fig. 8. Flowchart of the transient process for evaluating the container, PCM, and insulation temperatures of the receiver for a specified simulation time t_{max}.

$T_{p,mid}, T_{p,2}$, and $T_{c,2}$. $T_{p,mid}$ is the node between $T_{p,1}$ and $T_{p,2}$.

5.2. Material thermal analysis

In this investigation, the importance of the container, PCM, and insulation thermophysical parameters, as well as the environmental boundary condition, are analysed (Table 10). Each case is compared with the Baseline to determine the effects each variable has on the temperature.

Case 1 to 3 examines the variation of the specific heat and thermal conductivity of the container at room temperature and elevated temperatures. Comparing the Baseline with Case 4 and 5 determines the effect of using temperature-dependent specific heat and thermal conductivity versus constant values for the solid and liquid states of the PCM respectively, as proposed by [87,83]. The insulation is also a critical aspect of the high-temperature receiver to ensure mitigation of thermal losses. This reduction in loss allows for high performance of the propulsion system and constant operating conditions for the power system. The key insulation parameters investigated are the heat capacity and the thermal conductivity, Case 6 to 12. Lastly, the external temperature is analysed in Case 13 to determine the effect receiver placement has on the receiver. For example, internal (300 K) or external (3 K) location of the receiver relative to the spacecraft.

Each case is analysed over one orbit with the eclipse period commencing at 536 min into the orbit. There is no thermal power draw for the ORC and propulsion systems to isolate the effects of the material properties and environment temperatures on the charging and discharging of the TES system.

6. Influence of material thermal properties

Fig. 10 shows the temperature of the PCM and insulation nodes for

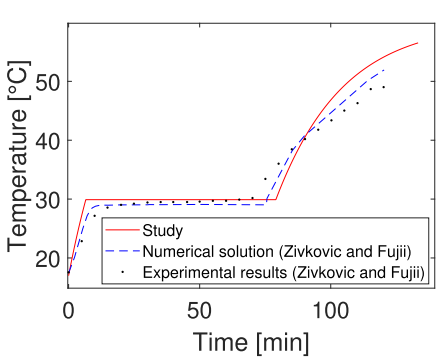

(a) Low-temperature melting case study

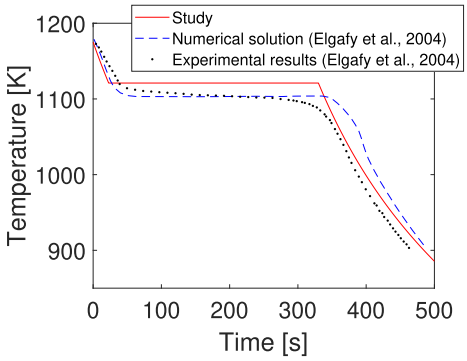

(b) High-temperature solidification case study

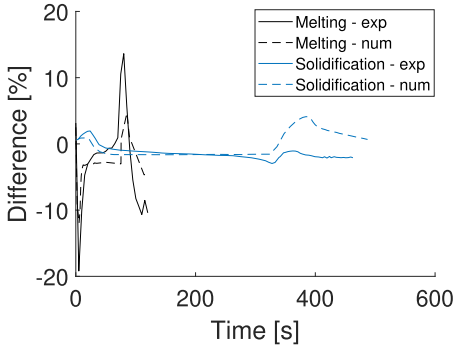

(c) Percentage error of the 2R1C PCM model.

Fig. 9. Validation results of the PCM against experimental data (exp) and a 2-dimensional numerical model (num) [92,95].

Table 9
List of the maximum absolute relative temperature percentage difference with respect to the average of the three simplified thermal resistance and capacitance models.

	$\lvert RD_{max}(T_{c,1})\rvert$ [%]			$\lvert RD_{max}(T_{p,mid})\rvert$ [%]			$\lvert RD_{max}(T_{c,2})\rvert$ [%]			Time step	Simulation time
	6R3C	4R2C	2R1C	6R3C	4R2C	2R1C	6R3C	4R2C	2R1C	[s]	[hours:min:sec]
6R3C	–	2.85	9.77	–	2.47	4.67	–	2.31	3.96	0.0002	04:36:48
4R2C	2.85	-	6.76	2.47	–	3.21	2.31	–	3.90	0.001	21:40
2R1C	9.77	6.76	–	4.67	3.21	–	3.96	3.90	–	0.01	03:59

$T_{p,mid}$ is the node between $T_{p,1}$ and $T_{p,2}$.

Table 10
Summary of design parameters for the material design investigation.

Case	c_{cont} [J/kgK]	$kcont$ [W/mK]	c_{pcm} [J/kgK]	k_{pcm} [W/mK]	c_{ins} [J/kgK]	k_{ins} [W/mK]	T_{ext} [K]
Baseline	1150	52	$f(T)$	$f(T)$	2000	0.33	300
1	793	52	$f(T)$	$f(T)$	2000	0.33	300
2	1150	20	$f(T)$	$f(T)$	2000	0.33	300
3	793	20	$f(T)$	$f(T)$	2000	0.33	300
4	1150	52	$c_l = c_s = 1040$	$f(T)$	2000	0.33	300
5	1150	52	$f(T)$	$k_s = 20$, $k_l = 60$	2000	0.33	300
6	1150	52	$f(T)$	$f(T)$	1	0.33	300
7	1150	52	$f(T)$	$f(T)$	100	0.33	300
8	1150	52	$f(T)$	$f(T)$	1000	0.33	300
9	1150	52	$f(T)$	$f(T)$	2000	0.25	300
10	1150	52	$f(T)$	$f(T)$	2000	0.69	300
11	1150	52	$f(T)$	$f(T)$	2000	CBCF 18–2000† : $f(T)$ (higher k)	300
12	1150	52	$f(T)$	$f(T)$	2000	CBCF 15–2000‡ : $f(T)$ (lower k)	300
13	1150	52	$f(T)$	$f(T)$	2000	0.33	3

‡ $k_{ins}(T) = -4.88 \times 10^{-14}T^4 + 3.255 \times 10^{-10}T^3 - 4.92 \times 10^{-7}T^2 + 5.229 \times 10^{-4}T + 0.1$ [54]

‡ $k_{ins}(T) = 1.139 \times 10^{-13}T^4 - 5.078 \times 10^{-10}T^3 + 1.013 \times 10^{-6}T^2 - 6.063 \times 10^{-4}T + 0.23$ [54]

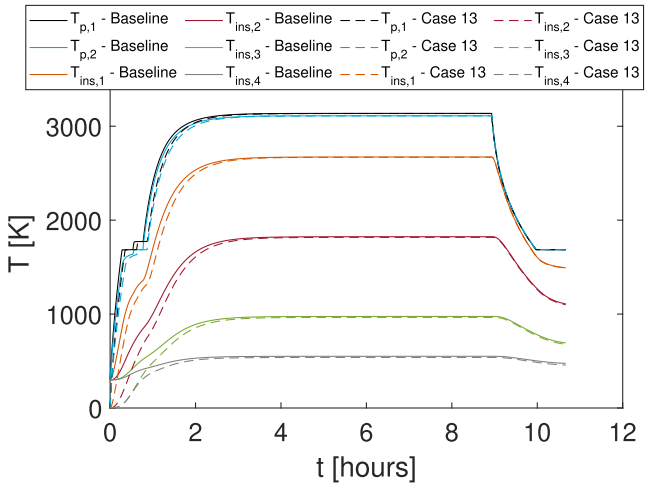

Fig. 10. Simulation temperature profile results of the Baseline case and Case 13 versus time for one orbit assuming a 640 min orbital period and a 104 min eclipse.

the Baseline case and Case 13, where the receiver is external to the spacecraft structure. The placement of the receiver affects the heating and cooling behaviour of the PCM, but has a minimal effect, $< 0.05\%$, on the maximum steady-state temperature obtained by the container and PCM (Table 12). For the outer insulation layer, the maximum relative percentage difference of the steady-state temperature is only 2.2% lower than the baseline value. Table 13 compares the time it takes the PCM to reach the mushy zone (i.e. when the node temperature reaches 1684 K), and the time it takes to complete the phase change (i.e. when the node temperature exceeds 1686 K). For Case 13, the PCM takes significantly longer to reach the phase change process with a maximum relative difference of 26%. Therefore, the environment boundary conditions have a significant influence on the heating profile of the PCM and the losses through the insulation. The results in Table 11 indicate that varying the specific heat and thermal conductivity of the container has a minimal effect on the temperature profiles. By reducing either the specific heat (Case 1 and 3) and thermal conductivity (Case 2 and 3), the container wall heats up and cools down at a faster rate. The variation of the maximum steady-state temperatures (Table 12) of the container, PCM, and outer insulation layer for Case 1 to 3 compared to the Baseline case is less than 0.05%. Results show that the relative time difference for all container simulations is a maximum of −0.31% deviation from the baseline value (Table 13). The negative relative difference means that by reducing the specific heat and thermal conductivity of the container, the phase change melts at a faster rate. Therefore, based on the minimal effect these thermophysical properties have on the temperature profile,

Table 12
List of the maximum relative percentage difference with respect to the Baseline case of the maximum steady-state temperature.

Case	$T_{c,1}$	$T_{p,1}$	$T_{p,2}$	$T_{c,2}$	$T_{ins,outer}$
Baseline [K]	3150	3137	3111	3098	550
	Percentage difference [%] relative to Baseline				
1	<1e−3	<1e−3	<1e−3	<1e−3	<1e−3
2	<1e−3	−0.01	−0.01	−0.04	−0.02
3	<1e−3	−0.01	−0.01	−0.04	−0.02
4	<1e−3	<1e−3	<1e−3	<1e−3	<1e−3
5	−0.01	0.02	0.07	0.10	0.03
6	<1e−3	<1e−3	<1e−3	<1e−3	<1e−3
7	<1e−3	<1e−3	<1e−3	<1e−3	<1e−3
8	<1e−3	<1e−3	<1e−3	<1e−3	<1e−3
9	1.91	2.01	2.20	2.30	−5.24
10	−8.2	−8.5	−9.2	−9.6	14.4
11	−10.1	−10.6	−11.4	−11.9	16.7
12	−8.1	−8.5	−9.2	−9.5	14.3
13	−0.04	−0.04	−0.04	−0.05	−2.18

Table 13
List of the maximum relative percentage difference relative to the Baseline case of the time at which the phase change (PC) commences and ends.

Case	Node P,1		Node P,2	
	$t_{start,PC}$	$t_{end,PC}$	$t_{start,PC}$	$t_{end,PC}$
Baseline [min]	16.8	32.2	33.0	46.2
	Percentage difference [%] relative to Baseline			
1	−0.22	−0.12	−0.12	−0.09
2	−0.09	−0.05	−0.05	−0.03
3	−0.31	−0.17	−0.17	−0.12
4	10.4	5.2	5.1	3.6
5	−0.80	−0.09	−0.18	−0.18
6	−21.9	−22.9	−23.4	−20.3
7	−19.4	−21.2	−21.8	−19.1
8	−6.8	−8.9	−9.2	−8.9
9	−5.6	−5.2	−5.2	−4.6
10	20.4	18.0	18.4	17.1
11	2.0	4.2	4.4	4.4
12	−8.1	−3.5	−3.6	−3.0
13	25.8	16.2	16.1	12.7

it is reasonable to assume a constant specific heat and thermal conductivity for the container when determining the transient behaviour of the system. By changing the solid PCM specific heat to a constant value (Case 4) the heating time of the first PCM node, $T_{p,1}$, is increased by 10%. However,there is almost no effect on the maximum steady-state temperature. Overall the most significant relative percentage difference in temperature between Case 4 and the Baseline case is −11% with the container and PCM temperatures being the most affected. This

Table 11
List of the maximum relative temperature percentage difference relative to the Baseline case over one orbit. Temperature values correspond with those defined in Fig. 7.

Case	$T_{c,1}$	$T_{p,1}$	$T_{p,mid}$	$T_{p,2}$	$T_{c,2}$	$T_{ins,1}$	$T_{ins,2}$	$T_{ins,3}$	$T_{ins,4}$
1	−3.37	0.29	1.08	0.32	0.32	0.12	0.07	0.05	0.02
2	2.47	0.13	0.99	0.11	−0.09	−0.16	−0.12	−0.08	−0.04
3	−3.06	0.42	1.15	0.42	0.35	−0.11	−0.08	−0.05	−0.03
4	−11.1	−11.0	−10.7	−10.5	−10.2	−7.1	−4.1	−2.2	−1.26
5	32.8	9.8	1.51	−9.8	−10.9	−4.04	−1.62	−0.72	−0.44
6	32.6	33.8	35.5	37.8	38.0	98.6	161.4	105.4	48.6
7	30.3	31.4	33.0	35.1	35.3	84.7	143.4	98.3	45.6
8	13.9	14.4	15.3	16.7	29.3	24.7	39.5	33.1	17.0
9	7.4	7.7	8.2	9.4	29.0	6.9	−11.1	−11.4	−8.5
10	−18.5	−19.0	−19.8	−20.8	−20.8	−18.1	29.1	34.5	27.2
11	−10.8	−11.0	−11.2	−11.5	−11.9	10.3	29.8	42.6	18.8
12	−8.6	−8.8	−9.0	−9.2	−9.5	−17.4	36.8	57.7	−16.8

$$RD_{\max}(T)_{\text{case}x} = \max\left(\frac{T(t)_{\text{case}x} - T(t)_{\text{baseline}}}{0.5[T(t)_{\text{case}x} + T(t)_{\text{baseline}}]}100\right) \text{ where } x = [1,\ldots,12]$$

considerable variation strengthens the need to include temperature-dependent specific heat values. The effect of using a constant solid and liquid thermal conductivity (Case 5) for the PCM is less than 0.1% on the relative difference in maximum steady-state temperature and less than 1% on the relative time difference to reach and complete the phase change. The small discrepancy is a result of the same change in the magnitude of the liquid and solid thermal conductivity. The small deviation in temperatures for the three models discussed in Section 5.1 could also be a result of this finding.

Table 11 highlights the large variation in temperature profiles when changing the specific heat capacity of the insulation (Case 6 to 8). However, the specific heat capacity of the insulation has a negligible effect of $< 0.001\%$, on the maximum steady-state temperature reached by all simulations. Therefore the thermal mass of the insulation does not need to be accounted for preliminary steady-state design calculations. A percentage difference of more than 20% is achieved when comparing the Baseline with Case 6 ($c = 1$ J/kgK) in terms of the time taken to reach the melting temperature from the start of the simulation. Increasing the specific heat increases the time to reach the phase change transition. For the constant insulation thermal conductivity simulations (Case 9, 10 and Baseline), the higher the thermal conductivity, the lower the steady-state temperature values due to the increase in losses from the insulation to the environment. The temperature-dependent insulation thermal conductivity results in Table 11 (Case 11 and 12), highlight the need for insulation materials with low thermal conductivity to get the best results (i.e. increase the receiver's rate of heating and minimise losses to the environment) as expected. The high variations in relative temperature differences strengthen the need to include temperature-dependent thermal conductivity of the insulation and include radial discretisation throughout the insulation to model the system with better accuracy. Case 12 (lower k_{ins}) results in the PCM getting heated up faster, reaching a higher maximum temperature and cooling down slower when compared to Case 11 (higher k_{ins}) due to the reduction in losses.

7. Final design

7.1. Design modification due to selection of PCM

Modification of the optimal geometry given in Table 4 is required for the final preliminary design due to the selection of Silicon as the PCM. An increase in the mass of the PCM is needed to ensure sufficient storage of the bi-modal system is possible. This increase was achieved by increasing the PCM diameter ratio. The PCM length remained constant to avoid the need for longitudinal discretisation by ensuring a low Biot number. Fig. 11 provides the results of increasing the PCM diameter ratio. The simulation assumes the ORC system continuously draws a constant thermal power of 2834 W from node *ins,1* after 50 min. The propulsion system draws a constant 59.16 kW of thermal power from node *p,1* for 620 s before the eclipse period begins (Fig. 12b). Increasing the diameter ratio to eight provides sufficient TES to keep the PCM near the melting temperature during the eclipse period. Diameter ratios below six did not provide adequate TES. Fig. 12 shows the temperature and thermal power of the eight diameter ratio receiver over five orbits.

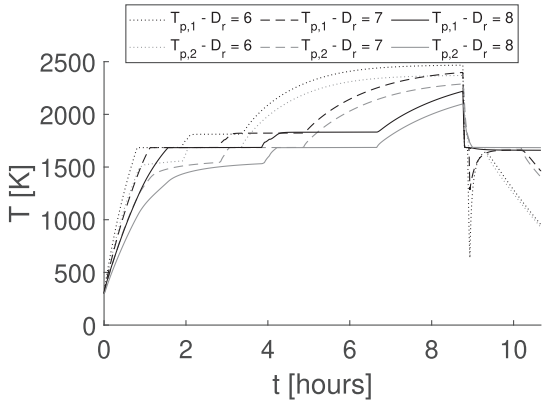

Fig. 11. Results of PCM temperature versus time for various outer-to-inner PCM diameter ratios.

The reduction in melting temperature of Silicon versus the optimal solution also reduces the specific impulse and therefore increases the propellant tank and propellant mass. For this design, the insulation is taken as CBCF 15–200 with temperature-dependent thermal conductivity, and the specific heat assumed to be 2 kJ/kg. The Silicon thermophysical properties used are the same as those provided in Table 7.

In addition, the optimal design resulted in a condenser design with 166 channels with a diameter of 0.368 mm necessary for condensation to occur at steady-state conditions. This results, in a condenser with a width and length of 0.15 m and 42.7 m and thus excessively large aspect ratio. Having a large condenser increases the risk of Micrometeoroid and Orbital Debris (MMOD) penetration, the complexity of system integration, and structural concerns. Therefore, for future optimisations, it is essential to add aspect ratio constraints for the condenser. The new condenser design layout proposed to meet the condensation requirement uses 16 channels with a diameter 1.2 mm, to produce a width and length of 5.5 m by 0.61 m. This design increases the mass and volume of the condenser by 3.84 kg and 0.0041 m^3 as well as the pressure drop by 1.53%.

Fig. 13a illustrates the major components of the pressure-fed STP system. The mass distribution of the components is presented in Fig. 13b. The margin is equivalent to 20% of the dry mass. The margin excludes the propellant as an additional 10% margin on the ΔV has been incorporated (STP-01 requirement). The results show that when this is the case, the wet bi-modal system mass is 75.8%.

7.2. Channel design configuration analysis

This analysis examines the influence of the channel design on the propellant heat transfer coefficient in terms of critical heat flux (CHF). This analysis assists in selecting a design that minimises the occurrence of the Inverted Annular Flow Boiling (IAFB) and Dispersed Flow Film Boiling (DFFB) regimes to obtain higher heat transfer coefficient.

The high wall temperature of the receiver could result in low/high-quality CHF regimes. If the CHF quality is low, boiling is divided into IAFB and DFFB regimes. If dryout occurs at high qualities, DFFB regime will be present after saturated boiling flow. IAFB and DFFB considerably reduce the heat transfer coefficient and thus increase the propellant tubing length required for sufficient heat transfer. Ways to minimise this in the design layout is to preheat the propellant by running the tubing inside layers of the insulation before getting into contact with the high-temperature PCM. However, this is neglected for this study to identify the worst-case operation modes.

A CHF analysis on the ORC system is provided in [52]. Therefore this analysis is extended to the propulsion system. In the ORC system investigation, the method proposed by [96] is implemented. However, for the propulsion case, it is not suitable as the propellant (water) operating conditions, mass flux and pressure, fall outside its validity range [97]. Thus, the CHF quality, x_{crit}, is determined using the method proposed by [98],

$$x_{crit} = 1.4We_{fo}^{0.03}P_R^{0.08} - 15.0\left(Bo\frac{P_H}{P_F}\right)^{0.15}Ca^{0.35}\left(\frac{\rho_g}{\rho_f}\right) \tag{31}$$

where We_{fo} is the liquid only Weber number, P_R is the reduced pressure, and Bo is the Boiling number. The wetted and heated perimeter of the channel are represented as P_F and P_H respectively. Ca is the Capillary number and ρ_g and ρ_f are the density of the vapor and liquid phase of the working fluid. The Bromley and the Bishop correlations are deemed suitable in terms of estimating the heat transfer coefficient of water for

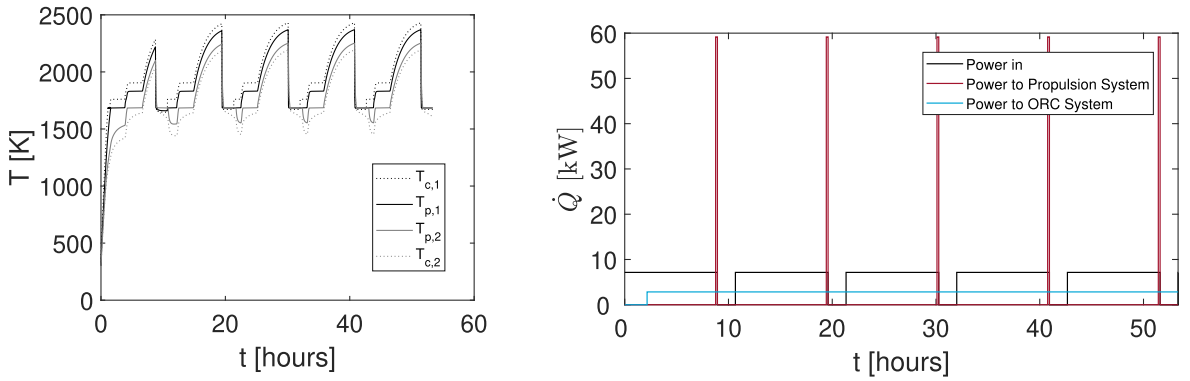

(a) PCM temperature versus time (b) Thermal power versus time

Fig. 12. Results of a bi-modal system with a Silicon PCM diameter ratio of 8 assuming constant thermal power draw for ORC and STP systems. The propulsion and ORC thermal power is assumed to be drawn from node *p,1* and *ins,1* respectively.

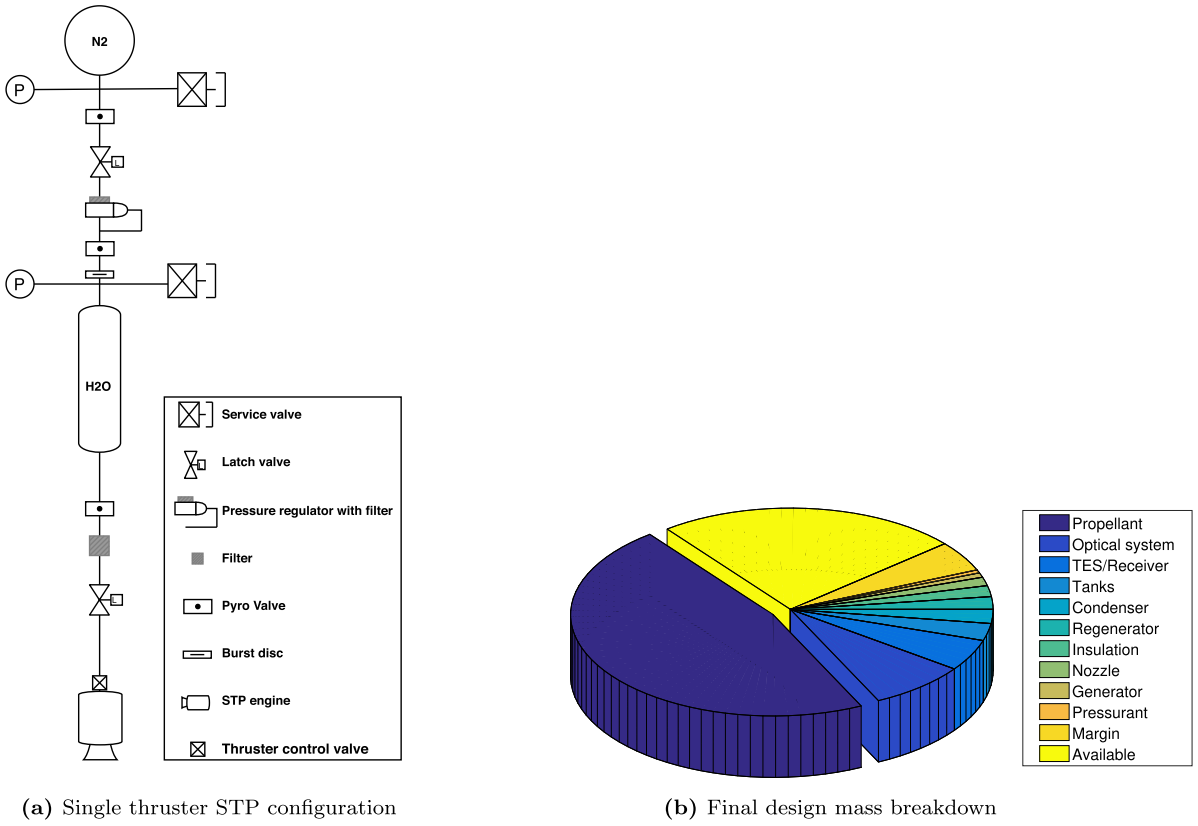

(a) Single thruster STP configuration (b) Final design mass breakdown

Fig. 13. Preliminary final design propulsion layout and component mass distribution.

the IAFB and DFFB regime respectively [52].

The channel designs analysed are spiral and straight configurations with circular channels. The spiral configuration consists of a single tube that spirals around the PCM's container, and the straight configuration consists of several straight channels that run along with the PCM's container due to ease of manufacture (compared to placing the channels inside the PCM). The maximum number of channels is constrained to the physical limit of channels, including wall thicknesses, that can be placed around the container. The maximum allowable length of the spiral tubing is equivalent to the axial length of the PCM container and the spiral tube having a pitch equal to its outer diameter. For this analysis, the entire surface area of the channel is assumed to be heated. The entire length of the tubing wall temperature is assumed to be equal to the outer container wall temperature. This assumption is acceptable due to the low Biot number of the current design, which allows the PCM to be modelled as a lumped-capacity model in the longitudinal direction. Future recommendations include a two-dimensional CFD analysis to provide higher fidelity modelling of the coupling-convective heat transfer between the propellant and PCM.

The range of channel diameters considered is between 0.19 and 6.5 mm to fall within the validity range of the heat transfer coefficient model [99]. The critical Reynolds number is taken as 2300 which falls within the critical transition range of macro- and micro-tubes [100–102]. However, future testing of the system is recommended as the critical Reynolds number in micro-tubes is an area of debate with low values less than 1500 [103] or broad range between 1200 to 3800 [104] reported.

7.3. Channel design results

Fig. 14 shows that dryout quality for both the spiral and straight propellant tube configuration. For the straight configuration, a reduction in the number of channels and size result in lower quality dryout values, as depicted in Fig. 14a. This region also corresponds to high mass flux ($G > 1608$ kg/m^2, Fig. 15a) which exceed the validity of the empirical correlations to calculate the two-phase boiling heat transfer coefficient. Larger diameters with more channels are desired to mitigate the chance of the flow entering the IAFB regime.

The length of the straight channel configuration is constrained to the length of the PCM. This short length together which large diameters lead to large Boiling numbers, $Bo > 44(10^{-4})$, indicated in Fig. 15b. These values exceed the validity of the empirical correlation used to calculate dryout quality. Therefore, the straight configuration is limited to channel diameters less than 1 mm with a minimum limit of 10 channels to meet the mass flux limit. The allowable mass flux restricts the lower limit of the channel diameter. Note, low channel diameters less than 0.51 mm are outside the range of validity for Eq. 31, although valid for the heat transfer coefficient equations.

The dryout incipience quality increases when approaching the top right corner of Fig. 14b for the spiral configuration. This increase is due to a decrease in mass flux, caused by an increase in channel diameter as indicated in Fig. 16a, and an increase in Boiling number, caused by an increase in channel length as illustrated in Fig. 16b. The Boiling number increases with increasing channel diameter, however, at a slower rate and therefore has less influence on the dryout quality than the reduction in mass flux.

For the spiral configuration channel diameters, less than 4 mm have substantial pressure drops, due to the increase in mass flux and long channel lengths, which result in infeasible designs as shown in Fig. 17. Additionally, the length of the spiral channel is restricted to between 1 and 3 m to avoid large pressure drops. To reduce the pressure drop that occurs in the straight channel configuration, larger diameters and higher channel numbers are necessary.

Fig. 18 provides the normalised propellant exit temperature to wall temperature of the container for the spiral and straight configuration. The results show that the spiral configuration can achieve higher propellant exit temperature ratios compared to the straight channel configuration for feasible designs.

8. Conclusion

The objective of this work is to investigate the feasibility of a novel integrated solar thermal system that can co-generate electricity and propulsion for small satellites. A comprehensive, innovative design approach for the proposed system was established to aid in developing feasible designs. The design approach highlights thirteen parameters needed to determine the primary system mass of the bi-modal system along with additional inputs such as the mission requirements, engineering constraints, and design choices. The approach is suitable to assist with future design evaluations of this system and can be easily extended to other missions and applications. A single-objective optimisation was performed using a genetic algorithm to minimise the overall wet system mass fraction to determine the feasibility of the system onboard small satellites. The models implemented have been validated against available experimental data where possible. Additional investigations were conducted to provide insight into the transient behaviour of the system and identify key parameters required to ensure the system is modelled sufficiently accurate.

The following conclusions and innovations can be drawn:

1. The optimisation results illustrate that for the GTO to Lunar orbit, the integrated solar thermal system is suitable for satellites that have a gross mass of 400 kg or 500 kg. For more reliable data, the complexity of the mass estimation models for the concentrator, water tank blowdown, insulation, and condenser design can be increased. The propellant mass accounts for 40 to 50% of the total mass fraction for the mini-satellites investigated. The concentrator and insulation contribute up to 8% and 7% of the total mass, respectively. Attractive features of the integrated system are high specific energy, fast transfer times, higher resistance to degradation, and a propulsion system with lower power consumption compared conventional systems and potentially lower cost. However, the disadvantage of the system is the low power density of around 10 W/kg; an order of magnitude lower than the future interplanetary target values.
2. Silicon was found to be the most suitable near-term PCM as it exceeds the specific energies (> 250 Wh/kg) required for future planned interplanetary missions. The optimal silicon receiver geometry provided low Biot numbers such that the PCM can be modelled as a lumped capacitance model.
3. For the dynamic behaviour of the receiver, the time percentage difference to heat the PCM to its melting temperature increases by 26% when placing the receiver external to the spacecraft. Although, the relative difference in the maximum steady-state temperature is only -0.04% and -2.2% for the PCM and outer insulation layer, respectively. The specific heat and thermal conductivity of the container have a minimal effect on the transient behaviour of the bi-modal system. The thermal conductivity also has a minimal effect on the maximum steady-state temperature and phase change timing. This effect is due to the PCM operating predominately in the two-phase and liquid phase during the orbit as well as the relatively small difference in thermal conductivity from room temperature to melting temperature. Conversely, the PCM specific heat has a large effect (up

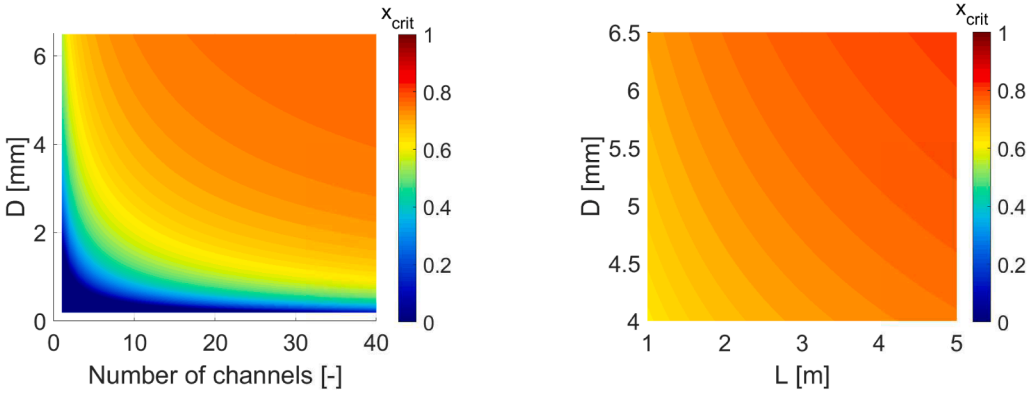

(a) Straight configuration (b) Spiral configuration

Fig. 14. Simulation results of the dryout incipience quality for various channel geometries.

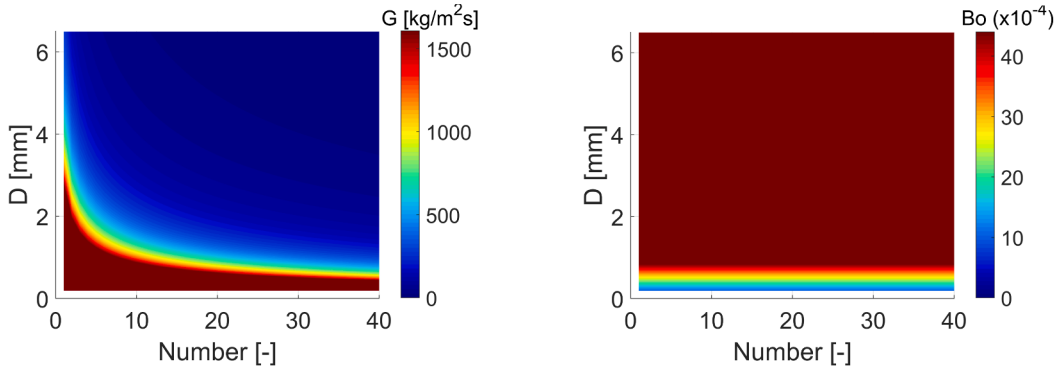

(a) Mass flux (b) Boiling number

Fig. 15. Simulation results of the flow parameters for the straight configuration.

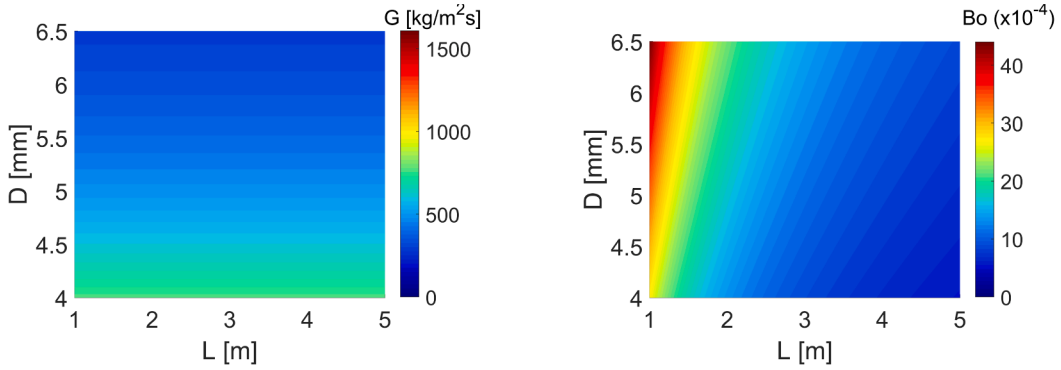

(a) Mass flux (b) Boiling number

Fig. 16. Simulation results of the flow parameters for the spiral configuration.

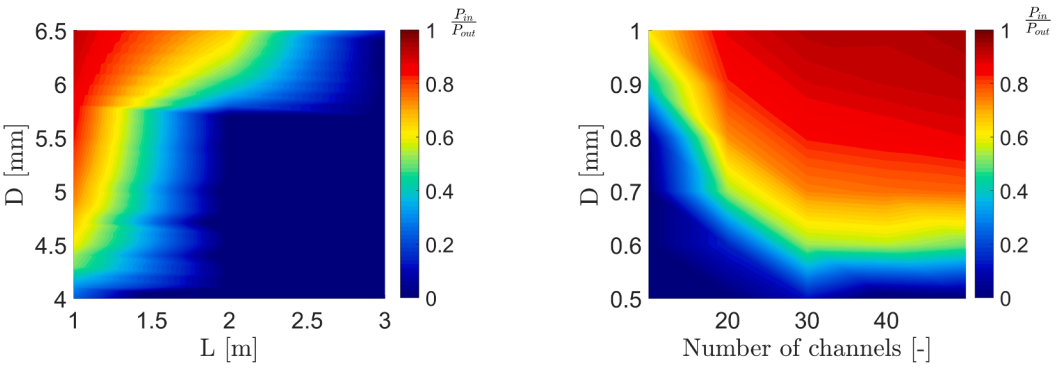

(a) Spiral configuration (b) Straight configuration

Fig. 17. Simulation results of the propellant input pressure with respect to the exit pressure for various channel geometries. The input pressure is 8.59 bar and the mass flow rate is 9.62 g/s.

to 10%) on the relative time percentage difference to reach the melting temperature, if a constant value is assumed. The insulation thermal conductivity and specific heat have a considerable influence on the time to reach the melting temperature, with relative differences up to 20% and 23% respectively in comparison to the baseline. Additionally, the insulation thermal conductivity has an 11.4% and 17% effect on the maximum steady-state temperature reached versus the baseline for the PCM and outer insulation layer position, respectively. Therefore, the temperature-dependent specific heat of the insulation and PCM and thermal conductivity of the insulation is essential for more accurate dynamic modelling of the bi-modal system.

4. The CHF should be examined at an early stage in the design process to identify the flow conditions of the propellant and improve the heat transfer. This guideline is due to the high operating temperatures of the receiver. Spiral channel configurations are better suited for the solar thermal system, due to the higher dryout incidence quality, which results in higher heat transfer coefficients than the feasible straight channel solutions.

The above conclusions provide key design guidelines for high-temperature bi-modal systems that integrate STP and ORC systems. Future work will be devoted to the improvement of the dynamic model of the system, specifically the convective coupling of the fluids with the

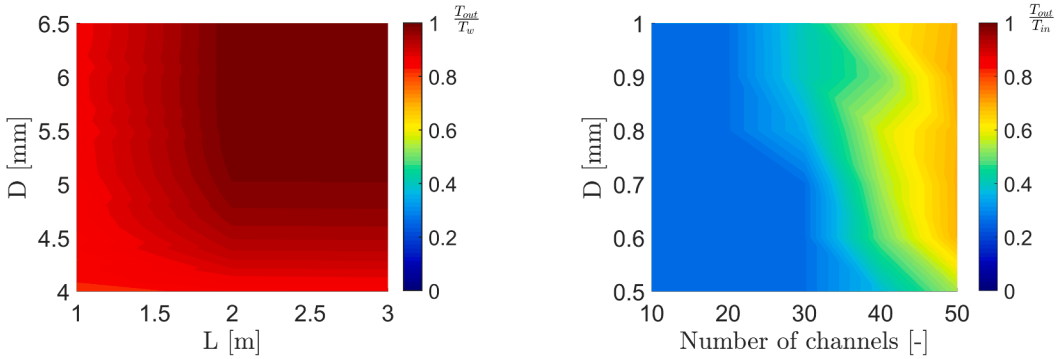

(a) Spiral configuration (b) Straight configuration

Fig. 18. Simulation results of the propellant exit temperature with respect to the wall temperature, which is taken as the melting temperature of the PCM for various channel geometries. The input pressure is 8.59 bar and the mass flow rate is 9.62 g/s.

receiver. Experimental testing is necessary to advance the bi-modal design and verify the predicted performance.

Declaration of Competing Interest

The authors declare that they have no known competing financial interests or personal relationships that could have appeared to influence the work reported in this paper.

References

[1] R. Surampudi, J. Blosiu, P. Stella, J. Elliott, J. Castillo, T. Yi, J. Lyons, M. Piszczor, J. McNatt, C. Taylor, E. Gaddy, S. Liu, E. Plichta, C. Iannello, Solar Power Technologies for Future Planetary Science Missions, Tech. rep., NASA, Pasadena, Califronia, 2017.

[2] R. Surampudi, J. Blosiu, R. Bugga, E. Brandon, M. Smart, J. Elliott, J. Castillo, T. Yi, L. Lee, M. Piszczor, T. Miller, C. Reid, C. Taylor, S. Liu, E. Plichta, C. Iannello, Energy Storage Technologies for Future Planetary Science Missions, Tech. rep., NASA, Pasadena, Califronia, 2017.

[3] M.D. Antonio, C. Shi, B. Wu, A. Khaligh, Design and Optimization of a Solar Power Conversion System for Space Applications, IEEE Trans. Industry Appl.

[4] K. Montgomery, J. Buckner, Z. Levin, J. Cromer, D. Wilt, Advanced Space Power Technology Development at the Air Force Research Laboratory, in: AIAA Scitech 2019 Forum, 2019, p. 1671.

[5] D.B. Scharfe, A.D. Ketsdever, A Review of High Thrust, High Delta-V Options for Microsatellite Missions, 45th AIAA/ASME/SAE/ASEE Joint Propulsion Conference 15 (2009) 1–14.

[6] F. Kennedy, Solar Thermal Propulsion for Microsatellite Manoeuvring, Phd thesis, University of Surrey (2004).

[7] F. Leverone, A. Cervone, E. Gill, Cost analysis of solar thermal propulsion systems for microsatellite applications, Acta Astronautica 155. doi:10.1016/j.actaastro.2018.11.025.

[8] C.F. Gartrell, A Future Solar Orbital Transfer Vehicle Concept, IEEE Trans. Aerospace Electronic Syst. AES 19 (5) (1983) 704–710, https://doi.org/10.1109/TAES.1983.309372.

[9] P. Henshall, P. Palmer, Concentrator Pointing Control Concept for Fiber Optic Augmented Solar Thermal Propulsion Systems, J. Spacecr. Rock. 53 (1) (2015) 230–234, https://doi.org/10.2514/1.A33352.

[10] R.M. Zubrin, T.K. Sulmeisters, M.G. Jacox, K. Watts, The integrated power and propulsion stage: A mission driven solution utilizing thermionic technology, in: AIP Conference Proceedings, Vol. 246, 1992, pp. 1259–1267. doi:10.1063/1.41747.

[11] K.K. Laug, M.R. Holmes, K.O. Westerman, Solar Bi-modal system concept: Mission applications, a preliminary assessment, in: AIP Conference Proceedings, Vol. 324, 1995, pp. 155–159. doi:10.1063/1.47232.

[12] K.K. Laug, M. Holmes, K.O. Westerman, R. Spickard, Solar bi-modal system concept: Common development issues with nuclear systems, in: AIP Conference Proceedings, Vol. 324, 1995, pp. 821–826. doi:10.1063/1.47121.

[13] J. Malloy, R. Rochow, J. Inman, Hybrid Solar Rocket Utilizing Thermal Storage for Propulsion and Electrical Power, Us patent 5,459,996, Patent and Trademark Office (1995).

[14] P. Frye, Integrated solar upper stage (ISUS) space demonstration design, in: Space technology and applications international forum (STAIF - 97), ASCE, 1997, pp. 461–466. doi:10.1063/1.52033.

[15] C.T. Kudija, P.E. Frye, Integrated Solar Upper Stage (ISUS) engine ground demonstration (EGD), in: AIP Conference Proceedings, Vol. 420, 1998, pp. 348–353. doi:10.1063/1.54818.

[16] T.L. Kassler, P. Frye, R. Partch, Solar thermal OTV - Applications to reusable and expendable launch vehicles, Acta Astronaut. 47 (2–9) (2000) 215–226, https://doi.org/10.1016/S0094-5765(00)00061-8.

[17] M. Gilpin, High Temperature Latent Heat Thermal Energy Storage to augment Solar Thermal Propulsion for Microsatellites, Ph.D. thesis, University of Southern California (2015).

[18] A.K. Hyder, R.L. Wiley, G. Halpert, D.J. Flood, S. Sabripour, Spacecraft power technologies, Vol. 1, Imperial College Press, London, 2000.

[19] M. Gilpin, D.B. Scharfe, M. Young, A. Pancotti, Molten boron phase-change thermal energy storage: containment and applicability to microsatellites, in: 42nd AIAA Thermophysics Conference, 2011.

[20] V.L. Teofilo, P. Choong, J. Chang, Y.-L. Tseng, S. Ermer, Thermophotovoltaic energy conversion for space, J. Phys. Chem. C 112 (21) (2008) 7841–7845.

[21] A. Datas, A. Martí, Thermophotovoltaic energy in space applications: Review and future potential, Sol. Energy Mater. Sol. Cells 161 (2017) 285–296, https://doi.org/10.1016/j.solmat.2016.12.007.

[22] T. Kessler, An overview of a solar thermal propulsion and power system demonstration applicable to HEDS, in: AIAA Space 2001 Conference and Exposition, AIAA SPACE Forum, American Institute of Aeronautics and Astronautics, kessler2001, 2001. doi:doi:10.2514/6.2001-4777. doi: 10.2514/6.2001-4777.

[23] G. Angelino, C. Invernizzi, E. Macchi, Organic working fluid optimization for space power cycles, in: Modern research topics in aerospace propulsion, Springer, 1991, pp. 297–326.

[24] E. Baldasso, M.E. Mondejar, J.G. Andreasen, K.A.T. Rønnenfelt, B.Ø. Nielsen, F. Haglind, Design of organic Rankine cycle power systems for maritime applications accounting for engine backpressure effects, Appl. Therm. Eng. 178 (2020) 115527, https://doi.org/10.1016/j.applthermaleng.2020.115527.

[25] X. Wang, E.K. Levy, C. Pan, C.E. Romero, A. Banerjee, C. Rubio-Maya, L. Pan, Working fluid selection for organic Rankine cycle power generation using hot produced supercritical CO2 from a geothermal reservoir, Appl. Therm. Eng. 149 (2019) 1287–1304, https://doi.org/10.1016/j.applthermaleng.2018.12.112, http://www.sciencedirect.com/science/article/pii/S1359431118354589.

[26] J. Freeman, I. Guarracino, S.A. Kalogirou, C.N. Markides, A small-scale solar organic Rankine cycle combined heat and power system with integrated thermal energy storage, Appl. Therm. Eng. 127 (2017) 1543–1554, https://doi.org/10.1016/j.applthermaleng.2017.07.163.

[27] D. Schubert, Mems-concept using micro turbines for satellite power supply, in: Solar Power, InTech, 2012, Ch. pp. 195–210.

[28] W.E. Mlurray, R.L. Gervais, Integration of Large Power Systems into Manned Space Stations, IEEE Trans. Aerospace Electron. Syst. AES 5 (2) (1969) 170–184, https://doi.org/10.1109/TAES.1969.309903.

[29] C. Toro, N. Lior, Analysis and comparison of solar-heat driven Stirling, Brayton and Rankine cycles for space power generation, Energy 120 (2017) 549–564.

[30] N. Muller, L.G. Fréchette, Performance analysis of Brayton and Rankine cycle microsystems for portable power generation, in: ASME 2002 International Mechanical Engineering Congress and Exposition, American Society of Mechanical Engineers, 2002, pp. 513–522.

[31] G. Angelino, C. Invernizzi, Cyclic methylsiloxanes as working fluids for space power cycles, J. Solar Energy Eng. 115 (3) (1993) 130–137.

[32] P. Colonna, E. Casati, C. Trapp, T. Mathijssen, J. Larjola, T. Turunen-Saaresti, A. Uusitalo, Organic Rankine cycle power systems: from the concept to current technology, applications, and an outlook to the future, Journal of Engineering for Gas Turbines and Power 137 (10).

[33] S. Lecompte, H. Huisseune, M. Van Den Broek, B. Vanslambrouck, M. De Paepe, Review of organic Rankine cycle (ORC) architectures for waste heat recovery, Renew. Sustain. Energy Rev. 47 (2015) 448–461.

[34] J.J. Soon, J.W. Chia, H. Aung, J.M. Lew, S.T. Goh, K. Low, A Photovoltaic Model Based Method to Monitor Solar Array Degradation On-Board a Microsatellite, IEEE Trans. Aerosp. Electron. Syst. 54 (5) (2018) 2537–2546, https://doi.org/10.1109/TAES.2018.2822081.

[35] J. Harinck, P. Colonna, A. Guardone, S. Rebay, Influence of thermodynamic models in two-dimensional flow simulations of turboexpanders, J. Turbomach. 132 (1) (2010) 11001.

[36] A. Uusitalo, T. Turunen-Saaresti, A. Guardone, A. Grönman, Design and flow analysis of a supersonic small scale ORC turbine stator with high molecular complexity working fluid, in: ASME Turbo Expo 2014: Turbine Technical Conference and Exposition, American Society of Mechanical Engineers, 2014, pp. V03BT26A004–V03BT26A004.

[37] J. Schiffmann, D. Favrat, Experimental investigation of a direct driven radial compressor for domestic heat pumps, Int. J. Refrig 32 (8) (2009) 1918–1928, https://doi.org/10.1016/j.ijrefrig.2009.07.006, http://www.sciencedirect.com/science/article/pii/S0140700709001686.

[38] J. Schiffmann, Integrated Design and Multi-objective Optimization of a Single Stage Heat-Pump Turbocompressor, Journal of Turbomachinery 137 (7). doi: 10.1115/1.4029123. doi: 10.1115/1.4029123.

[39] Newspace, Reaction wheels, accessed on 27 Septermber 2020 (2020). https://www.newspacesystems.com/portfolio/reaction-wheel/.

[40] F. Leverone, A. Cervone, E. Gill, Cost analysis of solar thermal propulsion systems for microsatellite applications, Acta Astronaut. 155 (2019) 90–110, https://doi.org/10.1016/j.actaastro.2018.11.025.

[41] F. Leverone, A. Cervone, M. Pini, E. Gill, Design of a Solar Thermal Propulsion and Power System for Mini-satellite Lunar Orbit Insertion, in: 2020 IEEE Aerospace Conference, 2020.

[42] J. Kreider, Medium and High Temperature Solar Processes, Energy Science and Engineering, Academic Press Inc, New York, 1979.

[43] P. Henshall, A Proposal to Develop and Test a Fibre-Optic Coupled Solar Thermal Propulsion System for Microsatellites, Tech. Rep. 0704–0188, Surrey University Guildford, United Kingdom (2006).

[44] J.E. Midwinter, Optical fibers for transmission, Wiley, New York, 1979.

[45] R.K. Shaltens, L.S. Mason, Early results from solar dynamic space power system testing, J. Propul. Power 12 (5) (1996) 852–858, https://doi.org/10.2514/3.24113.

[46] P. Frye, C. Kudija, Integrated solar upper stage engine ground demonstration test results and data analysis, in: 34th AIAA/ASME/SAE/ASEE Joint Propulsion Conference and Exhibit, 1998, p. 3958.

[47] H. Sahara, M. Shimizu, Solar Thermal Propulsion System for Microsatellites Orbit Transferring, in: 40th AIAA/ASME/SAE/ASEE Joint Propulsion Conference and Exhibit, 2004, https://doi.org/10.2514/6.2004-3764.

[48] J. Pearson Jr, P. Gierow, D. Lester, Near term in-space demonstration of an inflatable concentrator, in: 37th Aerospace Sciences Meeting and Exhibit, 1999, p. 1073.

[49] T. Nakamura, B.K. Smith, R.J. Gustafson, Solar Thermal Power System for Oxygen Production from Lunar Regolith: Engineering System Development, Joint Annual Meeting of LEAG, ICEUM, and SRR 1446 (2008) 95.

[50] J.R. Wertz, W.J. Larson, Space mission analysis and design, 3rd Edition, Microcosm Press, Torrance, California, 1999.

[51] T. Nakamura, D. Sullivan, J. McClanahan, J. Shoji, R. Partch, S. Quinn, Solar Thermal Propulsion for Small Spacecraft, in: 40th AIAA/ASME/SAE/ASEE Joint Propulsion Conference and Exhibit, no. July, 2004, pp. 1–11. doi:10.2514/6.2004-4138.

[52] F. Leverone, M. Pini, A. Cervone, E. Gill, Solar energy harvesting on-board small satellites, Renew. Energy 159 (2020) 954–972, https://doi.org/10.1016/j.renene.2020.05.176.

[53] T.L. Bergman, F.P. Incropera, D.P. DeWitt, A.S. Lavine, Fundamentals of heat and mass transfer, 7th Edition, John Wiley & Sons, 2011.

[54] Mersen, Rigid Carbon Insulation, accessed on 10 July 2019 (2020). https://www.mersen.com/products/graphite-specialties/carbon-insulation/rigid-carbon-insulation.

[55] D.L. Trimm, S. Akashah, A. Bishara, M. Absi-Halabi, Catalysts in Petroleum Refining 1989, Vol. 53 of Studies in Surface Science and Catalysis, Elsevier Science, 1990.

[56] P. Colonna, N.R. Nannan, A. Guardone, E.W. Lemmon, Multiparameter equations of state for selected siloxanes, Fluid Phase Equilib. 244 (2) (2006) 193–211.

[57] M. Preißinger, D. Brüggemann, Thermal stability of hexamethyldisiloxane (MM) for high-temperature organic Rankine cycle (ORC), Energies 9 (3) (2016) 183.

[58] F. Leverone, A. Cervone, M. Pini, E. Gill, P. Colonna, Feasibility of an integrated solar thermal power and propulsion system for small satellites, in: Proceedings of the International Astronautical Congress, IAC, Vol. 13, 2017.

[59] F. Leverone, M. Pini, A. Cervone, E. Gill, Feasibility of an On-board Micro-ORC System for Small Satellites, in: in: 5th International Seminar on ORC Power Systems, Athens, 2019.

[60] S. Bahamonde, M. Pini, C. De Servi, A. Rubino, P. Colonna, Method for the Preliminary Fluid Dynamic Design of High-Temperature Mini-Organic Rankine Cycle Turbines, J. Eng. Gas Turbines Power 139 (8) (2017) 82606.

[61] P. Colonna, T.P. der Stelt, FluidProp: a program for the estimation of thermo physical properties of fluids, http://www. FluidProp. com (2004).

[62] M. Moran, H. Shapiro, D. Boettner, M. Bailey, Fundamentals of engineering thermodynamics, John Wiley & Sons, 2010.

[63] P. Reynolds, William, Colonna, Vapor power plants, in: Thermodynamics, Ch. 7, Cambridge University Press, 2018.

[64] S. Kim, I. Mudawar, Universal approach to predicting two-phase frictional pressure drop for adiabatic and condensing mini/micro-channel flows, Int. J. Heat Mass Transf. 55 (11–12) (2012) 3246–3261.

[65] S. Kim, I. Mudawar, Universal approach to predicting heat transfer coefficient for condensing mini/micro-channel flow, Int. J. Heat Mass Transf. 56 (1–2) (2013) 238–250.

[66] D. Gilmore, Spacecraft thermal control handbook, Volume I: fundamental technologies, American Institute of Aeronautics and Astronautics Inc, 2002.

[67] A. Uusitalo, J. Honkatukia, T. Turunen-Saaresti, Evaluation of a small-scale waste heat recovery organic Rankine cycle, Appl. Energy 192 (2017) 146–158, https://doi.org/10.1016/j.apenergy.2017.01.088, http://www.sciencedirect.com/science/article/pii/S0306261917300995.

[68] G.P. Sutton, O. Biblarz, Rocket propulsion elements, John Wiley & Sons, 2016.

[69] G. Welsch, R. Boyer, E.W. Collings, Materials properties handbook: titanium alloys, ASM Int. (1993).

[70] D.H. Huang, D.K. Huzel, Modern engineering for design of liquid-propellant rocket engines, American Institute of Aeronautics and Astronautics (1992).

[71] E. Sato, S. Sawai, K. Uesugi, T. Takami, K. Furukawa, M. Kamada, M. Kondo, Superplastic titanium tanks for propulsion system of satellites, in: Materials science forum, Vol. 551, Trans Tech Publ, 2007, pp. 43–48.

[72] P. Olla, Space technologies for the benefit of human society and earth, Springer, Dordrecht, 2009.

[73] R.W. Larson, Wiley J and Henry, Gary N and Humble, Space propulsion analysis and design, McGraw-Hill, 1995.

[74] R. Biesbroek, G. Janin, Ways to the Moon, ESA bulletin 103 (2000) 92–99.

[75] M. Perryman, K. O'Flaherty, D. Heger, A. McDonald, The HIPPARCOS and TYCHO catalogues: The Hipparcos Satellite Operation, ESA Publications Division, 1997.

[76] D. Simon, Biogeography-Based Optimization, IEEE Trans. Evol. Comput. 12 (6) (2008) 702–713, https://doi.org/10.1109/TEVC.2008.919004.

[77] J.M. Ponce-Ortega, M. Serna-González, A. Jiménez-Gutiérrez, Use of genetic algorithms for the optimal design of shell-and-tube heat exchangers, Appl. Therm. Eng. 29 (2) (2009) 203–209, https://doi.org/10.1016/j.applthermaleng.2007.06.040, http://www.sciencedirect.com/science/article/pii/S1359431108001294.

[78] A.C. Caputo, P.M. Pelagagge, P. Salini, Heat exchanger design based on economic optimisation, Appl. Therm. Eng. 28 (10) (2008) 1151–1159, https://doi.org/10.1016/j.applthermaleng.2007.08.010, http://www.sciencedirect.com/science/article/pii/S1359431107002839.

[79] A.C. Caputo, P.M. Pelagagge, P. Salini, Joint economic optimization of heat exchanger design and maintenance policy, Appl. Therm. Eng. 31 (8–9) (2011) 1381–1392, https://doi.org/10.1016/J.APPLTHERMALENG.2010.12.033.

[80] R.M. Myers, S.R. Oleson, F.M. Curran, S.J. Schneider, Small satellite propulsion options, Technical Memorandum 106701, NASA, Lewis Research Cebter, 1994.

[81] E. Lemmon, M. Huber, M. McLinden, NIST REFPROP v9. 1 Reference fluid thermodynamic and transport properties (2013).

[82] MatWeb, The Online Materials Information Resource, http://www/matweb.com/ (2002).

[83] A. Datas, M. Zeneli, C. del Cañizo, I. Malgarinos, A. Nikolopoulos, N. Nikolopoulos, S. Karellas, A. Martí, Molten silicon storage of concentrated solar power with integrated thermophotovoltaic energy conversion, in: AIP Conference Proceedings, Vol. 2033, AIP Publishing LLC, 2018, p. 90005.

[84] M. Zeneli, I. Malgarinos, A. Nikolopoulos, N. Nikolopoulos, P. Grammelis, S. Karellas, E. Kakaras, Numerical simulation of a silicon-based latent heat thermal energy storage system operating at ultra-high temperatures, Appl. Energy 242 (2019) 837–853, https://doi.org/10.1016/j.apenergy.2019.03.147, http://www.sciencedirect.com/science/article/pii/S0306261919305562.

[85] C. Prakash, M. Samonds, A.K. Singhal, A fixed grid numerical methodology for phase change problems involving a moving heat source, Int. J. Heat Mass Transf. 30 (12) (1987) 2690–2694, https://doi.org/10.1016/0017-9310(87)90152-9.

[86] J.Z. Alvi, Y. Feng, Q. Wang, M. Imran, J. Alvi, Modelling, simulation and comparison of phase change material storage based direct and indirect solar organic Rankine cycle systems, Appl. Therm. Eng. 170 (2020) 114780, https://doi.org/10.1016/j.applthermaleng.2019.114780, http://www.sciencedirect.com/science/article/pii/S1359431119321982.

[87] A. Datas, A. Ramos, A. Martí, C. del Cañizo, A. Luque, Ultra high temperature latent heat energy storage and thermophotovoltaic energy conversion, Energy 107 (2016) 542–549.

[88] NIST, Silicon, accessed on 10 Septermber 2020 (2018). URL https://webbook.nist.gov/cgi/inchi?ID=C7440213&Type=JANAFS&Plot=on.

[89] J.J. Valencia, P.N. Quested, Thermophysical properties.

[90] A. Veeraragavan, L. Montgomery, A. Datas, Night time performance of a storage integrated solar thermophotovoltaic (SISTPV) system, Solar energy 108 (2014) 377–389.

[91] G. Xiaohong, L. Bin, G. Yongxian, Y. Xiugan, Two-dimensional transient thermal analysis of pcm canister of a heat pipe receiver under microgravity, Appl. Therm. Eng. 31 (5) (2011) 735–741.

[92] B. Zivkovic, I. Fujii, An analysis of isothermal phase change of phase change material within rectangular and cylindrical containers, Solar energy 70 (1) (2001) 51–61.

[93] A.J. Rulison, W.-K. Rhim, Constant-pressure specific heat to hemispherical total emissivity ratio for undercooled liquid nickel, zirconium, and silicon, Metall. Mater. Trans. B 26 (3) (1995) 503–508.

[94] Z. Zhou, S. Mukherjee, W.-K. Rhim, Measurement of thermophysical properties of molten silicon using an upgraded electrostatic levitator, J. Cryst. Growth 257 (3–4) (2003) 350–358.

[95] A. Elgafy, O. Mesalhy, K. Lafdi, Numerical and experimental investigations of melting and solidification processes of high melting point PCM in a cylindrical enclosure, J. Heat Transfer 126 (5) (2004) 869–875.

[96] M.M. Shah, Comprehensive correlation for dispersed flow film boiling heat transfer in mini/macro tubes, Int. J. Refrig 78 (2017) 32–46, https://doi.org/10.1016/J.IJREFRIG.2017.03.019.

[97] M. Shah, Improved general correlation for CHF in uniformly heated vertical annuli with upflow, Heat Transfer Eng. 37 (6) (2016) 557–570.
[98] S. Kim, I. Mudawar, Universal approach to predicting saturated flow boiling heat transfer in mini/micro-channels - Part I. Dryout incipience quality, Int. J. Heat Mass Transf. 64 (2013) 1226–1238, https://doi.org/10.1016/J.IJHEATMASSTRANSFER.2013.04.016.
[99] S. Kim, I. Mudawar, Universal approach to predicting saturated flow boiling heat transfer in mini/micro-channels -w Part II. Two-phase heat transfer coefficient, Int. J. Heat Mass Transf. 64 (2013) 1239–1256, https://doi.org/10.1016/J.IJHEATMASSTRANSFER.2013.04.014.
[100] K.V. Sharp, R.J. Adrian, Transition from laminar to turbulent flow in liquid filled microtubes, Exp. Fluids 36 (5) (2004) 741–747.
[101] M. Lorenzini, G.L. Morini, S. Salvigni, Laminar, transitional and turbulent friction factors for gas flows in smooth and rough microtubes, Int. J. Therm. Sci. 49 (2) (2010) 248–255, https://doi.org/10.1016/j.ijthermalsci.2009.07.025.
[102] S. Barlak, S. Yapici, O.N. Sara, Experimental investigation of pressure drop and friction factor for water flow in microtubes, Int. J. Therm. Sci. 50 (3) (2011) 361–368, https://doi.org/10.1016/j.ijthermalsci.2010.08.018.
[103] G.M. Mala, D. Li, Flow characteristics of water in microtubes, Int. J. Heat Fluid Flow 20 (2) (1999) 142–148.
[104] C.-Y. Yang, Friction characteristics of water, R-134a and air in small tubes, Microscale Thermophys. Eng. 7 (4) (2003) 335–348, https://doi.org/10.1080/10893950390243608.
[105] James Blanchard, Target temperature prediction for plasma source ion implantation. J. Vacuum Sci. Technol. B: Microelectron. Nanometer Struct. Process., Measure. Phenomena 12 (2) (1994) 910–917, https://doi.org/10.1116/1.587326.